Composite Structures 389 (2026) 120384

Contents lists available at ScienceDirect

Composite Structures

journal homepage: www.elsevier.com/locate/compstruct

A validated finite element framework to realise the potential of thermoelastic stress analysis for quantitative studies of laminated CFRP structures

Riccardo Cappello [a,*], Rafael Ruiz-Iglesias [a,d], Giuseppe Pitarresi [b], Giuseppe Catalanotti [c], Janice M. Dulieu-Barton [a]

[a] Bristol Composites Institute (BCI), School of Civil, Aerospace and Design Engineering, University of Bristol, Bristol BS8 1TR, United Kingdom
[b] Department of Engineering, University of Palermo, Viale delle Scienze, Palermo 90128, Italy
[c] Faculty of Engineering and Architecture, Kore University of Enna (UKE), Cittadella Universitaria, Enna 94100, Italy
[d] Facultad de Ciencias Experimentales (Faculty of Experimental Sciences) Universidad Francisco de Vitoria, UFV, Edificio E (Francisco de Vitoria University), Ctra. M-515 Pozuelo-Majadahonda Km 1, 800 28223, Pozuelo de Alarcón, Madrid, Spain

ARTICLE INFO

Keywords:
Thermoelastic stress analysis
Composite materials
Non-adiabatic behaviour
Finite element modelling
Model validation

ABSTRACT

Quantitative Thermoelastic Stress Analysis (TSA) of laminated carbon fibre reinforced polymer (CFRP) structures poses a significant challenge, as the stress induced temperature change, caused by the thermoelastic effect, is influenced by heat transfer. Both in-plane and through the thickness heat conduction occurs, which is mainly driven by the step changes in the stresses at the ply interfaces in a multidirectional laminate. In most materials cyclic loading at sufficiently high frequencies minimises heat transfer. However, because of the large degree of anisotropy in both the thermal and mechanical properties of CFRP, adiabatic conditions do not occur at achievable loading frequencies. To understand the thermomechanical coupling in CFRP, a comprehensive experimental evaluation of an existing meso-scale finite element (FE) model that is able to reproduce the thermoelastic heat source ply-by-ply, is presented. Hence, a validated modelling framework is created that enables quantitative TSA to be carried out on CFRP structural components. It is established that the model is able to accurately predict the effects of different loading frequencies, layups, resin-rich regions and the effect of the necessary matt black paint surface layer. The modelling approach is demonstrated through a challenging experimental validation followed by application on a typical quasi-isotropic laminate. A practical application is presented, where a CFRP component with unknown material properties is assessed to demonstrate the utility of the modelling framework.

1. Introduction

The thermoelastic effect [1] is a reversible physical phenomenon that links linear elastic deformation to temperature changes. Thermoelastic Stress Analysis (TSA) is a well-established full-field, non-contact technique that exploits this thermomechanical coupling to enable quantitative evaluation of the stress state of a solid under linear elastic conditions [2]. For an orthotropic material, the relationship between temperature change, ΔT, and stress state, was first established in the 1980 s [3]. For fibre reinforced polymer composites ΔT can be expressed in terms of principal material directions (1,2) parallel and transverse to fibre direction as follows [3]:

$$\Delta T = -\frac{T_o}{\rho C_p}(\alpha_1 \Delta\sigma_1 + \alpha_2 \Delta\sigma_2) \quad (1)$$

where T_o is the absolute mean temperature of the test specimen, ρ is the density, C_p is the specific heat at constant pressure, α_1, α_2 are the coefficients of thermal expansion (CTE) and $\Delta\sigma_1, \Delta\sigma_2$ the stress changes.

ΔT is obtained using an image series obtained from an infra-red camera to provide a full-field visualisation across a region of interest in a structure. A detailed review of the types of cameras used for TSA and the image processing algorithms is provided in [4]. As an IR camera views the surface of a component the stress perpendicular to the traction free surface is neglected, hence Eq. (1) is expressed in terms of plane stress. Eq. (1) is only valid when isentropic conditions prevail, usually

* Corresponding author.
E-mail address: riccardo.cappello@bristol.ac.uk (R. Cappello).

https://doi.org/10.1016/j.compstruct.2026.120384
Received 7 November 2025; Received in revised form 23 March 2026; Accepted 23 April 2026
Available online 6 May 2026

achieved by cyclically loading the component at sufficient rate to minimise heat transfer. In laminated composite structures ΔT in each ply is dependent on the stacking sequence and materials used. To achieve adiabatic conditions, cyclic loading is typically applied. For quantitative analysis heat transfer should be avoided, but with carbon fibre reinforced polymers (CFRP), this can be difficult to achieve at realistic loading frequencies (up to 30 Hz) [5–9]. Section 2 of the paper provides a brief review of the complexity of applying TSA to CFRP structures. Notwithstanding the challenges associated with heat transfer, TSA has great potential in the analysis of CFRP components, as it can be deployed with minimal set-up requirements and component preparation, as well as its ability to provide, in a matter of seconds, full-field visualisation of the stress distributions in operating structures. Therefore, the overarching aim of the present paper is to demonstrate that the previously devised FEM (Finite Element Method) modelling framework [9] can be used to support quantitative TSA of CFRP components. Hence, a detailed experimental validation of the proposed modelling framework is described, using test specimens manufactured from the very well characterised IM7/8552 [10] CFRP material.

The surface resin rich layer (RRL) commonly found on composite structures can be incorporated into the model [9], so the effect of changing the RRL thickness on the thermoelastic response is examined both experimentally and in the model. Uniquely, the validated modelling framework, presented in the paper, offers the opportunity to probe the possibility of creating the "strain witness effect" [11,12] in CFRP materials.

In previous investigations, e.g. [7,13] it has been noted that the surface paint layer commonly applied in thermographic analyses has an effect on the thermoelastic response from composite materials, which changes with loading frequency. Hence, a further novel aspect of the present investigation is incorporating the paint layer into the modelling framework.

The key objectives and novel aspects of the work described in the paper are:

- Provide a comprehensive experimental validation of the modelling framework [9] incorporating for the first time the paint coating utilised in thermographic studies (Sections 3 to 6).
- Demonstrate how the validated FEM-model framework can be used to generate the thermoelastic response of each ply in a laminate stack and inform the surface measurements (Section 7).
- Use the validated FEM-model framework to systematically study the effect of the RRL and the paint coating (Section 8).
- Conduct a study that demonstrates the utility of the validated FEM-model by providing some application guidelines on a typical quasi-isotropic layup and a CFRP coupon extracted from a structural component, with a complex layup and unknown material system and therefore uncharacterised material properties (Section 9).

2. Brief review of application of TSA to CFRP laminates

Eq. (1) is derived from the heat diffusion equation (HDE) [14,15] where the balance between heat generation and mechanical work can be expressed as:

$$\rho C_\varepsilon \dot{T} - k\nabla^2 T = D_m + T\frac{\partial \sigma_{ij}}{\partial T}\dot{\varepsilon}_{ij} + T\rho\frac{\partial^2 H}{\partial T \partial \boldsymbol{\xi}}\dot{\boldsymbol{\xi}} + \dot{q}_s \tag{2}$$

where C_ε is the specific heat at constant strain, k is the thermal conductivity, H is the Helmholtz free energy potential, ξ is the internal state variable, D_m is the intrinsic mechanical dissipation, $\dot{q}_s$ is the quantity of heat transferred to the surroundings, and σ_{ij}, and ε_{ij} are the stress and strain tensors.

In Eq. (2) the term $T\frac{\partial \sigma_{ij}}{\partial T}\dot{\varepsilon}_{ij}$ defines the reversible thermoelastic coupling, which is the basis of TSA. The term $T\rho\frac{\partial^2 H}{\partial T \partial \boldsymbol{\xi}}\dot{\boldsymbol{\xi}}$ represents additional internal heat sources associated with changes in the internal variables, which along with D_m can be neglected for small deformations associated with linear elastic behaviour, i.e. well below that where plasticity and damage can evolve. In TSA it is generally the case that the temperature of the surroundings is very close to that of the specimen (ΔT is ca mK), so $\dot{q}_s$ can also be neglected. Additionally, if an infinitesimal material volume is considered, the spatial heat conduction term $k\nabla^2 T$ can be neglected, leaving only the thermoelastic coupling term $T\frac{\partial \sigma_{ij}}{\partial T}\dot{\varepsilon}_{ij}$. By utilising the material constitutive equations that describe the stress–strain and temperature relationships Eq. (1) is obtained. Noting that a further assumption is made that the elastic constants are independent of temperature, which is the case for CFRP materials at around room temperature, i.e. the usual conditions for TSA. For cases where the the elastic constants are sensitive to temperature, Wong et al. [16] defined a thermoelastic parameter that depends on the applied mean stress and the variation of the terms of the stiffness matrix with temperature. The theory was validated through agreement between predicted and experimental results for two metal alloys. It was shown that if the elastic constants are sensitive to temperature changes at room temperature, it is identified by an additional component in the thermoelastic response that occurs at twice the loading frequency, which was referred to as a 'higher order' thermoelastic response. The derivation of Eq. (1) from the thermoelastic coupling is well-established and derived in detail in several publications, e.g., [2].

For TSA of CFRP laminated composite structures the heat conduction term in Eq. (2) cannot be neglected. The individual plies that make up CFRP structures inherently have a high degree of anisotropy because of differences in the CTEs and the elastic constants [13]. In multidirectional laminated CFRP structures, the anisotropy results in step changes in ΔT that occur ply-by-ply, which drive heat transfer. Hence, the individual plies act as independent heat sources, producing variable thermoelastic responses through the thickness [5–9]. Given the thin thicknesses typical of CFRP prepregs plies (e.g., 0.127 mm for IM7/8552 [10]), the temperature response measured on the external surface is influenced by significant through-thickness heat diffusion, even at higher loading frequencies [5,7,17,18]. Significant effort has been invested to interpret the thermoelastic response from CFRP composites from experiments on a variety of laminated composite materials; these were described in detail in [7]. In general, three different propositions were made, based on classical laminate theory and strain compatibility ply by ply, to identify the source of the thermoelastic response, as follows:

- ***The global laminate response*** [6,7,19] is based on the overall mechanical and thermal response of the laminate. This is valid at low loading frequencies (typically below 5 Hz), where the thermal diffusion length allows heat transfer through the entire laminate. Hence, an experimental calibration of the relationship between the measured ΔT value and the stress experienced by the entire laminate can be made, as demonstrated in [7,19]. The work described in the present paper, provides a means of identifying the loading frequency at which the global laminate response is generated and the potential for quantitative TSA on structural scale CFRP components.
- The ***surface ply response*** [6–8,12,17,20,21] is based on the concept that the ΔT comes from only a thermally isolated ply on the surface of a component. Depending on stacking sequence, and with a relatively thin surface resin layer, it is shown that it is possible to isolate the surface ply response at moderate loading frequencies (e.g., around 10 to 20 Hz) in CFRP components. However, during many composite manufacturing processes, a relatively thick surface resin layer is generated, so the effect of the surface resin rich layer is explored in detail. It is demonstrated that, with careful tuning of the loading frequency, a response that is directly related to the stress in the surface ply can be obtained. In the present paper the FEM model

shows this is only possible for thin surface resin layers, re-establishing the validity of Eq. (1).

- The ***strain witness approach*** [6–8,12,22,23] stems from the existence of a resin rich surface layer, where the ΔT is based on the strain from the surface ply being transmitted in to the surface resin layer. Hence, the thermoelastic response can be calibrated in terms of the strain in the surface ply. The assumption is that when the resin is sufficiently thick there is no heat transfer to the surfaces. In the present paper it is demonstrated that for CFRP laminates, depending on stacking sequence, unrealistically thick surface resin layers would be required to make the strain witness assumption valid. Moreover, most of the studies have been conducted on specimens loaded in uniaxial tension, where it can be assumed the ply by ply strains are identical; this would not be the case where a component experiences bending or multiaxial loading.

In [7] the validity of each of the formulations and approaches and their limitations was investigated for GFRP and CFRP specimens loaded in uniaxial tension. The results showed that for GFRP laminates, heat transfer was limited and the source of the thermoelastic response was the surface resin layer [7,11]. Conversely, the CFRP laminates were affected by heat transfer for the laminates where step changes occurred in the ply-by-ply stresses. Here, a clear transition from the global laminate response at low loading frequencies (5 to 15 Hz) to the surface ply response for higher loading frequencies (15 to 30 Hz) was observed. In contrast, for lay-ups where the ply-by-ply stresses were uniform, there was no discernible change in thermoelastic response with loading frequency.

The first attempts to model the non-adiabatic behaviour in CFRP composites were reported in the early nineties, with analytical models being proposed in [5] and [18]. These methods were based on the finite difference solution of the one-dimensional heat diffusion equation, incorporating internal thermoelastic heat sources. The discretised solution enabled the prediction of through-thickness thermal behaviour and its dependence on loading frequency. However, these analytical approaches rely on simplifying assumptions such as infinite plate geometries and uniaxial loading conditions, which limit their applicability to real-world composite structures.

Recently [9], a FEM-based approach has been introduced that allows the 3-D heat conduction developed during cyclic loading to be incorporated into predictions of ΔT, enabling the evaluation of complex geometries. In the model the analytical derivation of the thermoelastic source term is performed locally and neglects the spatial heat conduction ($k\nabla^2 T$). However, if in the numerical implementation the FE mesh is sufficiently refined and solved over a small time discretisation, the heat diffusion term in Eq. (2) is included in the FEM model. As the modelling framework is used in the present paper details of its implementation are provided in Section 5.

In [9] the FEM model was verified against the 1-D conduction model developed in [5] for uniaxial tension stress states. Clearly an experimental validation is desirable, but this depends on a detailed knowledge of material properties, whereas in the numerical verification the same material properties could be used in both the analytical and FEM models. To reduce uncertainties in the FEM model, in the present paper the very well characterised CFRP IM7/8552 [10] is used to manufacture test specimens. Despite being well characterised there is still significant variation in the properties of IM7/8552. A detailed examination of the variation in the properties of IM7/8552 from many literature sources is reported in [13]. It was found that the CTEs provided the greatest source of uncertainty in predicting the thermoelastic response. Hence, in [13] an inverse approach is devised that enables identification of the CTEs by using TSA results from multi-directional composites. The material property values given in [13] including the derived CTEs, are used in the validation study detailed in the present paper and summarised in the following section of the paper.

A key motivation for the work described in the present paper is the recent advances in infrared (IR) sensor technology that have increased the application range for TSA's. Low-cost microbolometer-based sensors [4,24–26] have made the proposition of multi-camera TSA financially viable for large structural tests. The validated modelling framework proposed in the following sections of the paper will provide a means for rapid quantitative evaluation of structural behaviour, including serving as a tool for understanding the effect of heat transfer in TSA studies of large scale CFRP structures. In structural applications loads can only be applied at low frequencies, so adiabatic conditions cannot be achieved. An example of the application of the FEM-model is provided in [27], where the thermomechanical coupling of a steel T-joint under multiaxial fatigue loading was studied. Non-adiabatic behaviour was triggered by the combination of the relatively low loading frequency (1 Hz) and the non-uniform stress distribution, both in plane and through the thickness of the structure, due to the simultaneous application of compression, bending and shear. As the relevant material properties for steel are well known, the application of the FEM-model was a relatively straightforward prospect. A comparison of the ΔT derived from the TSA and the FEM model showed good agreement for the loading frequencies used in the experiment. However, there was little thermal conduction occurring in the experiment and small discrepancies between the experimental and numerical data sets were attributed to paint coating. The findings of [27] have prompted the further investigations, described in the present paper, utilising the validated modelling framework into the effect on the thermoelastic response of (i) a variety of CFRP stacking sequences with complex heat transfer, (ii) of varying the RRL and (iii) the inclusion of different paint coating thickness.

3. Test specimens and materials

Panels of IM7/8552 carbon fibre/epoxy prepreg [10] (nominal ply thickness of 0.127 mm) were manufactured in an autoclave following the recommended cure cycle and vacuum bagging procedure. Three cross-ply configurations $[0/90]_{3s}$, $[90/0]_{3s}$, and $[\pm 45]_{3s}$, and two multidirectional laminates $[0/0/0/45/\text{-}45/0]_s$ and $[0/45/\text{-}45/0/0/0]_s$ were produced. The cross ply and multidirectional panels were manufactured using different manufacturing techniques to provide different surface resin layer thicknesses. The $[0/90]_{3s}$, $[90/0]_{3s}$, and $[\pm 45]_{3s}$ panels were manufactured with only peel ply on the bag side of the laminate, so that a thin surface layer was produced on the mould side without the peel ply imprint, following the procedure implemented in [7]. The panels are characterized by a "smooth" side, with low RRL thickness, and a "rough" side, where the peel ply sits, with a thicker and irregular RRL. It has been noted, e.g. [7], that the peel ply imprint, in addition to modifying the thermoelastic response, has a deleterious effect in DIC, as the regular pattern causes aliasing to occur during the image correlation. Moreover, the rough pattern causes reflections, which exacerbate the effect of motion in TSA. It is therefore absolutely vital that the test specimens have a smooth surface. Hence the $[0/0/0/45/\text{-}45/0]_s$ and $[0/45/\text{-}45/0/0/0]_s$ panels were produced with a caul plate on the bag side of the lay-up. While the use of the caul plate has the advantage of generating two smooth surfaces, it does not allow for the excess resin to redirect to one of the surfaces. Therefore, the two smooth surfaces have a thicker surface resin rich layer (RRL). Test specimens were cut from the panels as rectangular strips with dimensions given in

Table 1
Test specimen geometry and RRL thickness.

Layup	Geometry (L × W × T) [mm]	RRL Thickness [μm]
$[0/90]_{3s}$	220 × 20 × 1.62	1.73 ± 1.10
$[90/0]_{3s}$	220 × 20 × 1.62	1.73 ± 1.10
$[\pm 45]_{3s}$	220 × 20 × 1.62	1.49 ± 1.32
$[0/0/0/45/\text{-}45/0]_s$	220 × 25 × 1.62	37.88 ± 4.48
$[0/45/\text{-}45/0/0/0]_s$	220 × 25 × 1.62	17.70 ± 6.88

Table 1.

Optical microscopy was used on small samples cut from the plates, to assess the thickness of the RRL for each specimen. Given the critical influence of the RRL on the thermoelastic response, it is essential to model this layer with the highest possible accuracy. For each specimen, 10 measurements were taken at different locations across the sample, and the average RRL thickness was determined. The average RRL thicknesses and their standard deviation measured from each tested specimen, and used later as input in the model, are also reported in Table 1. As the RRL is very thin for the cross-ply laminates, the distribution of the fibre in the resin has a strong influence on the thickness of the RRL and hence the large values of the standard deviation. It can be seen that the multidirectional laminates have a very large resin rich layer compared to the cross ply laminates. The RRL on the $[0/0/0/45/-45/0]_s$ specimen is more than twice as thick as the $[0/45/-45/0/0/0]_s$, the reasons for which are unknown. In these cases the standard deviation is much less than that of the cross-ply laminates. The end result is that two specimens were produced that provide a good basis for investigating the effect of varying RRL. It also demonstrates how the RRL can vary in two nominally identical manufacturing processes.

Although IM7/8552 is well characterised there exists a large variation in properties reported in the literature. In [13], an extensive survey and analysis was carried out and properties were down selected to define an inverse procedure for establishing the CTEs of IM7/8552 from the thermoelastic response. The material properties used in the present work are identical to those used in [13] and are listed in Table 2, specifying whether they were experimentally determined or taken as an average from the literature values [7,28–33] when direct experimental characterisation was not feasible. Two sets of CTEs are provided in [13], one using the inverse procedure on unpainted specimens over a frequency range of 0.5–30 Hz, and the other considering only low loading frequencies (0.5–5 Hz) from painted samples; these are referred to as $CTEs_1$ and $CTEs_2$, respectively, throughout the remainder of the paper. Interested readers are referred to [13] for a more detailed description of the material properties and the inverse procedure for obtaining the CTEs and to the curve fitting for obtaining the through thickness thermal conductivity, k_3. The properties of the 8552 epoxy resin, used to model the RRL are given in Table 3.

4. Experiments for model validation

Five specimens were tested in uniaxial cyclic tension–tension using an Instron Electropuls E10000 electrodynamic testing machine. The applied stresses over the laminate cross-sectional area are given in Table 4, which were tailored to the stacking sequence and laminate thickness, ensuring each specimen remained below the First Ply Failure (FPF) load. The experimental protocol described in [7] was replicated, using a greater variety of laminate stacking sequences. A broader range of loading frequencies (0.5–30.1 Hz – see Table 4) was employed to increase the number of data points and improve the robustness of the frequency-dependent analysis. The choice of using only balanced and symmetric laminates in the validation study is that these generate a variety of heat transfer conditions without the added experimental complexity of dealing with out-of-plane distortions that introduce uncertainty in the experimental results. Moreover, balanced and symmetric laminates are used in the vast majority of composite structures.

Table 2
Material properties for IM7/8552[13].

Property	Value	Source
Young's modulus E_1 (GPa)	161.33 ± 5.89	Measured [13]
Young's modulus E_2 (GPa)	10.29 ± 1.33	Measured [13]
Poisson's ratio ν_{12}	0.32 ± 0.0125	Measured [13]
Shear modulus G_{12} (GPa)	5.15 ± 0.25	Literature [7,28–33]
Shear modulus G_{23} (GPa)	4 ± 0.2	Literature [7,28–33]
$CTEs_1$ (α_1, α_2) (10^{-6} K^{-1})	−0.085 ± 0.003, 29.05 ± 2.59	Inverse procedure [13] unpainted specimens
$CTEs_2$ (α_1, α_2) (10^{-6} K^{-1})	−0.073 ± 0.006, 27.5 ± 2.23	Inverse procedure [13] painted specimens
Thermal conductivity k_1 (W m K^{-1})	4.89 ± 1.12	Literature [7,28–33]
Thermal conductivity $k_2 = k_3$ (W m K^{-1})	0.615 ± 0.13	Curve fitting [13]
Density (kg m^{-3})	1569 ± 22.1	Literature [7,28–33]
Specific heat C_p (J kg^{-1} K^{-1})	884.53 ± 45.1	Literature [7,28–33]

Table 3
Material properties for the 8552 epoxy resin[13].

Property	Value
Young's modulus E (GPa)	4.38 ± 0.47
Poisson's ratio ν	0.36 ± 0.03
Shear modulus G (GPa)	1.45 ± 0.04
CTE α_r (10^{-6} K^{-1})	49.4 ± 6.99
Thermal conductivity k (W m K^{-1})	0.25 [34]
Density (kg m^{-3})	1251 ± 69.53
Specific heat C_p (J kg^{-1} K^{-1})	1110 ± 55.5

Table 4
Load amplitude and frequency for each test specimen.

Layup	Cyclic Stress Mean ± Amplitude [MPa]	Target strain amplitude []	Loading frequencies [Hz]
$[0/90]_{3s}$	104.78 ± 89.06	1750	1.1, 3.1, 5.1, 7.1, 10.1, 12.1, 15.1, 20.1, 22.1,25.1, 27.1, 30.1
$[90/0]_{3s}$	94.30 ± 81.20	1590	
$[\pm45]_{3s}$	52.39 ± 39.29	4250	
$[0/0/0/45/-45/0]_s$	123.46 ± 111.11	2050	0.5, 1.1, 2.1, 3.1, 4.1, 5.1, 6.1,7.1,8.1,9.1,10.1, 12.1, 15.1, 17.1, 20.1, 22.1,25.1, 27.1, 30.1
$[0/45/-45/0/0/0]_s$	123.46 ± 111.11	2050	

Digital Image Correlation (DIC) [35] was used to obtain the strain amplitude value, to input in the numerical model, instead of relying on nominal load values from the testing machine. Note that the values given in Table 4 represent the target values; the actual measured values are provided in Table A1. Thus removing a significant source of uncertainty from the models. The smooth side of the specimens were imaged using a combined DIC and TSA setup. Previous studies have demonstrated that a thin white speckle pattern on a black background does not significantly influence the thermoelastic response [7]. Hence, a thin layer (ca. 10 μm) of matt black paint was applied to the specimen surface, followed by white speckles deposited using spray paint, for the DIC analysis. The infra-red image series for the TSA was captured using a Telops FAST M3K thermal camera equipped with a 50 mm lens. The camera operated at a frame rate of 383 Hz, acquiring 6000 images per test. The M3k camera has a Noise Equivalent Temperature Difference (NETD) below 18 mK. The system calibration is performed by the manufacturer and periodically verified in-house using a calibrated temperature controlled black body.

Specimen motion was corrected by tracking four aluminium fiducial markers, with a different emissivity to the paint, positioned at the corners of the specimens [36]. A subpixel image registration was employed to correct the displacements in each frame using the *imwarp* function in MATLAB. After which, the corrected thermal images were processed pixel by pixel using an in-house least-squares lock-in procedure by applying a least squares fit to the following expression [4]:

$$T(x,y,t) = T_0 + 0.5\Delta T(x,y,t)\cos\left(2\pi f_0 t + \varphi\right) \tag{3}$$

where f_0 is the loading frequency, φ is the phase of ΔT with respect to the applied load (acquired using the IR camera and time stamped with each captured IR image) and t is time.

A commercial MatchID [37] stereo DIC system was employed to synchronise image capture and process the data, enabling full-field displacements measurements of the specimens. A pair of FLIR Blackfly white-light cameras, each equipped with a 12 Mpx sensor and 25 mm lenses, were used to acquire the images. The white light images were recorded under the same cyclic loading conditions employed for the TSA analysis, but with a camera frame rate of 10 Hz, with a total of 316 images captured. The strains provided by the DIC were processed by employing a lock-in DIC (LIDIC) approach [38] by fitting to Equation (3), where temperature is replaced by strain. Hence, full-field strain fields were obtained under cyclic loading conditions, without the need of an accurate synchronisation and triggering with the load signal.

Fig. 1 presents the full-field thermoelastic response for the different CFRP configurations at various loading frequencies (1.1, 5.1, 10.1, 20.1, and 30.1 Hz). For the $[0/90]_{3S}$ specimen shown in Fig. 1 (a), the thermoelastic response in the 0° ply is lower than in the 90° subsurface ply due to differences in stiffness, CTEs, and stress distributions; since $\Delta T/T_0$ is greater in the 90° subsurface ply, heat is transferred to the surface at lower loading frequencies. However, as the frequency increases, the response becomes more adiabatic, and thermal conduction from the subsurface to the surface is limited. The patterns observed in the full-field plot at low and high frequencies differ: at low frequencies, a combination of longitudinal (0°) features from the surface ply and horizontal (90°) features from the subsurface ply can be identified. As the frequency increases, these horizontal patterns are no longer visible due to limitations in heat transfer through the thickness. It is important to note that the effect of the distribution of the fibre in the resin, as discussed in section 3, is very evident at all loading frequencies as a result of the thin RRL and the large difference between the thermoelastic response from the resin and the fibre in the 0° orientation.

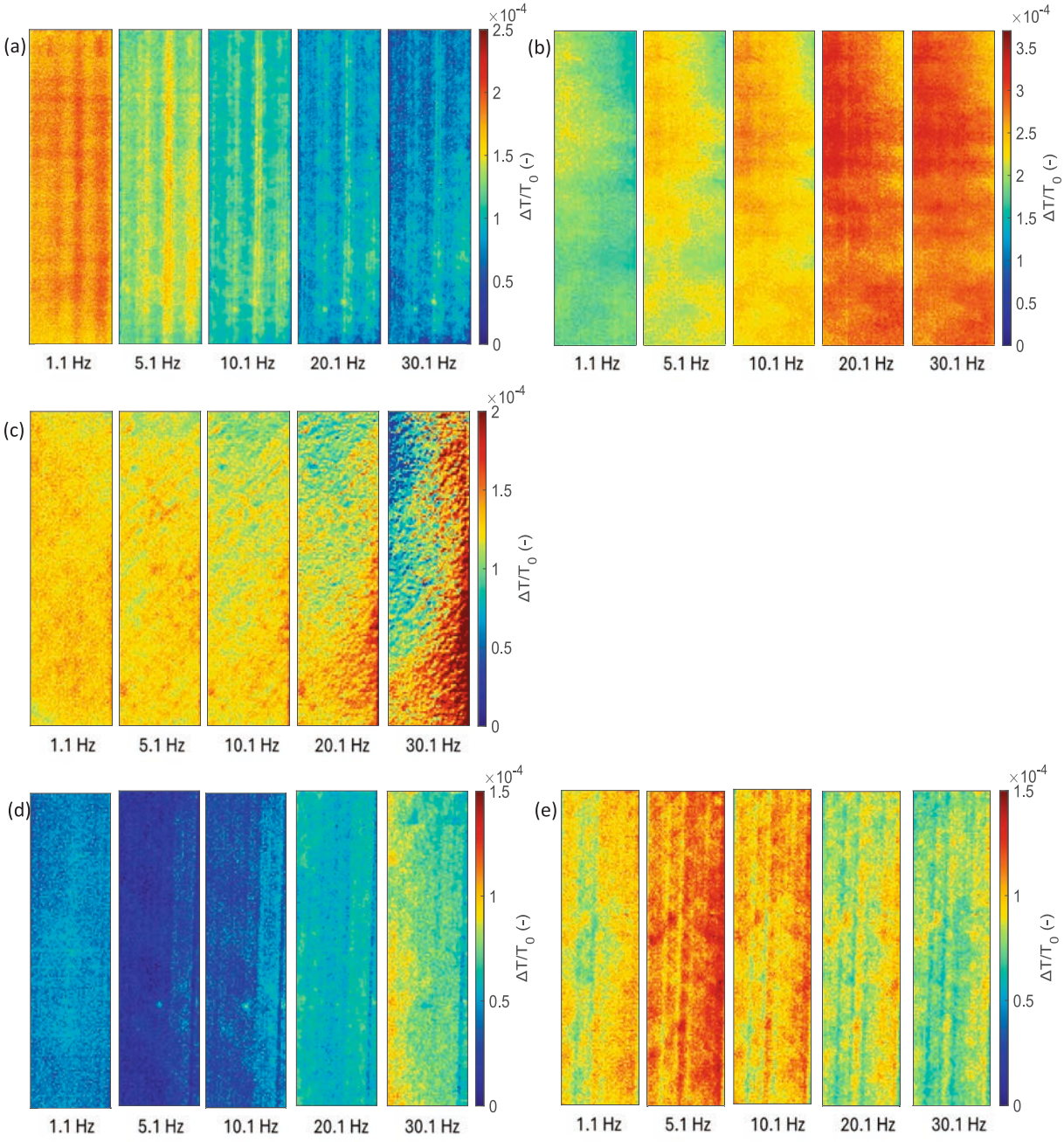

Fig. 1. Full-field $\Delta T/T_0$ extracted from a thermal image series (see Eq. (3)) captured at the cyclic stress levels given in Table 4 of (a) $[0/90]_{3S}$, (b) $[90/0]_{3S}$, (c) $[\pm 45]_{3S}$, (d) $[0/45/\text{-}\ 45/0/0]_S$, and (e) $[0/0/0/45/\text{-}45/0]_S$ specimens.

For the $[90/0]_{3S}$ specimen shown in Fig. 1 (b), $\Delta T/T_0$ decreases at low loading frequencies, because heat is being transferred from the surface ply to the subsurface ply. Both longitudinal and horizontal patterns are again visualised at low frequencies and only horizontal at high frequencies. At 1.1 Hz, the initial amplitude is the same for both cross-ply specimens, with $\Delta T/T_0 \approx 2 \times 10^{-4}$ indicating that sufficient time is available for heat diffusion, and hence the thermoelastic response is homogenised throughout the laminate. As the frequency increases, $\Delta T/T_0$ rises due to the reduced heat transfer from the 90° surface ply to the underlying subsurface layer. Although the RRL is thin, the distribution of fibres in the resin is not as evident as the $[0/90]_{3S}$ specimen, because the thermoelastic response from the 90° fibre orientation is closer to that of the resin.

For the $[\pm 45]_{3S}$ specimen in Fig. 1 (c), the stress induced temperature change is identical ply-by-ply and consequently adiabatic behaviour prevails. However, differences in the $\Delta T/T_0$ distributions are observed across the tested frequencies. At 1.1 Hz, $\Delta T/T_0$ appears to be practically homogeneous across the surface. At 5.1 and 10.1 Hz, distinct 45° patterns emerge, aligned with the fibre orientation, but once again not as evident as the $[0/90]_{3S}$ specimen, because the thermoelastic response from the 45° fibre orientation is closer to that of the resin. At 20.1 and 30.1 Hz, a temperature gradient becomes noticeable in the lower-right corner of the specimen, which becomes more pronounced with increasing frequency, which could be attributed to viscoelastic heating of the resin.

$\Delta T/T_0$ is shown for the $[0/45/\text{-}\ 45/0/0/0]_S$ and $[0/0/0/45/\text{-}45/0]_S$ specimens in Fig. 1 (d) and (e) respectively. At 1.1 Hz there is little evidence of fibres, indicating that the response is homogenised through the laminate because of heat transfer. For the $[0/45/\text{-}\ 45/0/0/0]_S$ specimen from 5.1 Hz there is clear evidence of both the surface ply and the 45° subsurface ply in all the images. For the $[0/0/0/45/\text{-}45/0]_S$ specimen the response is more homogeneous as a result of the three 0° plies at the surface. However, at almost every loading frequency the 45° plies are revealed, demonstrating the ability of TSA to detect subsurface features. It is clear from Fig. 1 (d) and (e) the response is more homogeneous across the specimens as a result of the thicker RRLs, but the 0° plies are more apparent in Fig. 1 (e) as the $[0/45/\text{-}45/0/0/0]_s$ specimen had the thinner RRL.

To provide a clear illustration of the effects described above a spatial average of $\Delta T/T_0$ was determined over approximately 13,700 datapoints taken from the central section of the test specimens, along with the corresponding standard deviation. Fig. 2 shows the spatial average of $\Delta T/T_0$ and phase for all the stacking sequences studied. The values of $\Delta T/T_0$ are of the order of 10^{-4}. This level of fidelity is achieved through the lock-in processing, which enables temperature differences to be resolved that are of the order 1 mK [24]; as T_0 is around 293 K the reported $\Delta T/T_0$ are small but measurable. For the $[0/90]_{3S}$ specimen and $[90/0]_{3S}$ specimen shown in Fig. 2 (a) and (b), the general variations with frequency described above are well defined and echo the trends observed in [7], with a clear transition from non-adiabatic conditions to adiabatic conditions occurring at around 20 Hz. The phase plots are interesting, despite the negative CTE value for α_1 the phase value is consistently around 175 degrees for the $[0/90]_{3S}$ specimen, up to 20 Hz after which the value increases to 180°. In contrast for $[90/0]_{3S}$ specimen the values are consistent at 180°. In [13] it was shown that the phase in a UD 0° lay-up was closer to zero. In the cross ply configuration, the constraining effect of the subsurface 90° ply induces a positive transverse stress in the 0° ply. Thus rendering the bracketed term in Eq. (1) positive, which produces a negative temperature change and a 180° phase shift between the load and temperature; this is discussed in more detail in section 6. The greater scatter in the response from the $[0/90]_{3S}$ specimen confirms that the variation in the RRL is more significant for this configuration than the $[90/0]_{3S}$. An important outcome from the tests on the $[0/90]_{3S}$ and $[90/0]_{3S}$ specimens is that the results replicate exactly the findings of [7], which were conducted in a different laboratory, using a different test machine and IR camera. The outcome confirms the repeatability and reproducibility of the findings despite a different set of environmental conditions.

For the $[\pm 45]_{3S}$ specimen, shown in Fig. 2 (c), the average response is practically constant apart from a small decrease evidenced at low frequencies. However there is considerable scatter in the data as the frequency increases, caused by the localised heating evidenced in the full-field images of $\Delta T/T_0$. The phase values remain constant at 180° up to around 15 Hz, after which an increase is observed, consistent with the possible onset of viscoelastic behaviour; this is also discussed in more detail in section 6. Tests were also conducted on identical $[\pm 45]_{3S}$ specimens in [7] but with a lower load, these followed the same trend as the present study but without the departure in standard deviation at the larger loading frequencies. This result also confirms to some extent the reproducibility of the results.

For the $[0/0/0/45/\text{-}\ 45/0]_S$ specimen shown in Fig. 2 (d) the thermoelastic response initially increases up to 4 Hz and then the response decreases. For the $[0/45/\text{-}\ 45/0/0/0]_S$ specimen shown in Fig. 2 (e), there is an initial decrease in thermoelastic response up to a frequency of around 4 Hz, followed by a marked increase in the response. In contrast to the cross ply specimens the phase is not close to 180°, but closer to zero, indicating a dominance of the 0° plies. Here the constraining effect of the 45° is insufficient to generate a large transverse stress, hence the negative α_1 controls the response. For the $[0/0/0/45/\text{-}\ 45/0]_S$ specimen the phase values settle at around −50°. For the $[0/45/\text{-}\ 45/0/0/0]_S$ specimen the phase decreases initially and then increases followed by a rapid decrease, settling at around −100°. It should be considered that both specimens have a very thick RRL and that this is strongly influencing the phase alongside the thermal interactions between surface and subsurface plies. The FEM model can provide a detailed insight and interpretation of the behaviour, which will be discussed in more detail in section 6.

5. Numerical modelling framework

The FEM model mesh used for all the laminate types, shown in Fig. 3, was constructed in Abaqus standard (implicit) using 3640 C3D8T elements (coupled temperature displacement) and 4725 nodes. A representative length (10 mm) of each of the specimens was modelled, making use of mid-plane symmetry, to support computational efficiency. The five laminate stacking sequences given in Table 1 were simulated ply by ply, with 4 elements per ply as shown in Fig. 3 (b); the same number of through thickness partitions were also employed for the RRL and the paint layer. This was sufficient to provide a detailed representation of the through thickness temperature gradients, while keeping computational times reasonable. Material properties were assigned to each component of the model as provided in Tables 2, 3 and 5. Even though the well characterised IM7/8552 CFRP material was selected to validate the model, there remain uncertainties in the material property values as indicated by the standard deviations provided in Tables 2, 3 and 5. The rigorous approach adopted in [13] to establishing the material properties means uncertainties are minimised. The most uncertain material parameter, α_1, with a variation of over 200% found from several literature sources reported in [13], was identified in [13] with a precision of less than 10% (see Table 2). Clearly these uncertainties will have an effect on the predicted values of $\Delta T/T_0$ and the phase angle.

The RRL was modelled as a uniform layer using the average thickness value given in Table 1, as it would be computationally very expensive to replicate the variations in the RRL reported in Table 1. Incorporating the paint is a new feature of the model framework, it does not contribute to the structural response but is known to cause thermal damping. The paint was assigned a thickness of 10 μm, which is typical for TSA [39], and was treated as a passive thermal layer to simulate the thermal damping, with small mechanical properties. In preliminary studies, the thin RRL at the ply interfaces were included and found to have no effect on the surface response, so to reduce computational expense these were

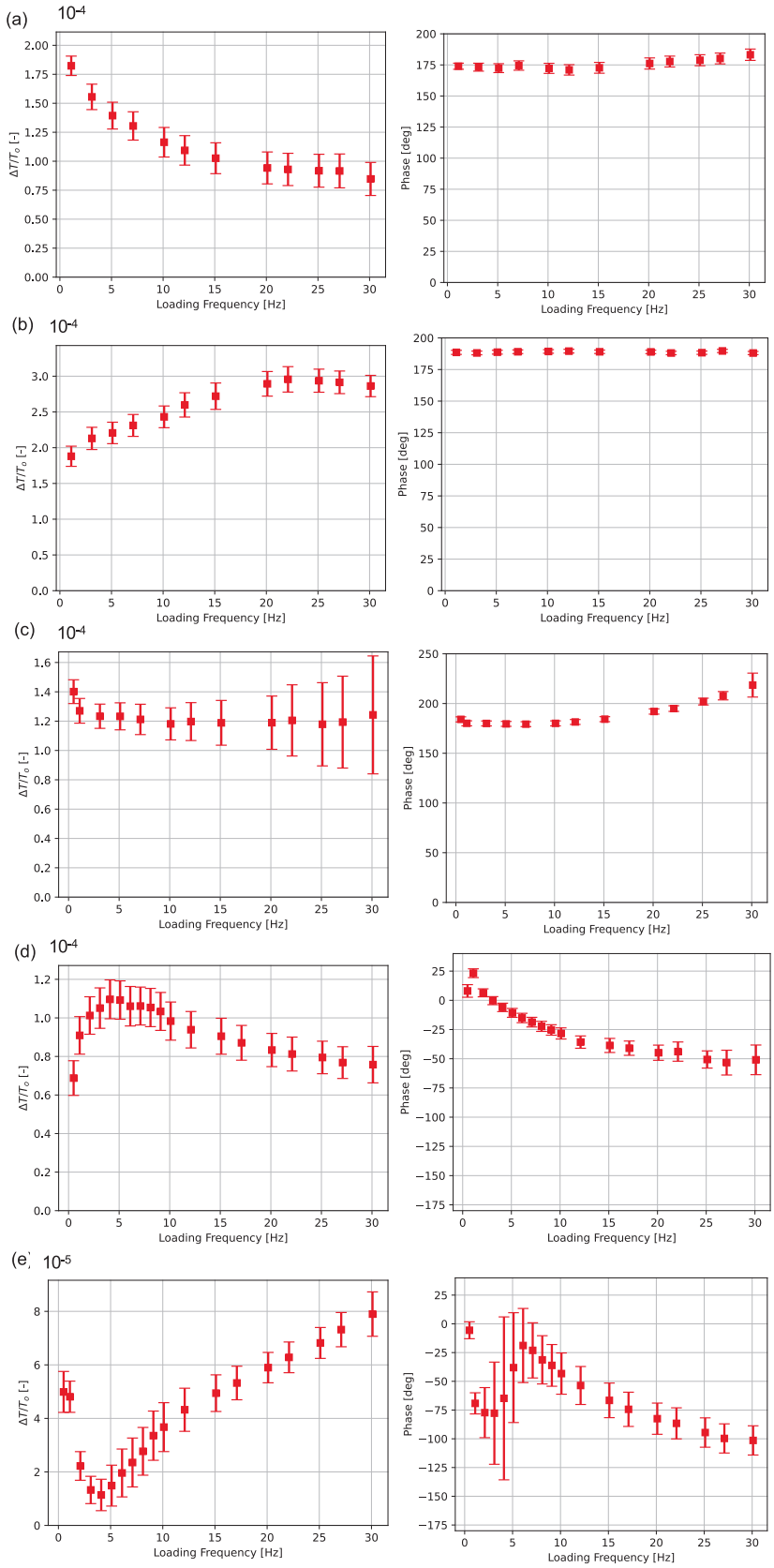

Fig. 2. AVG $\Delta T/T_0$ and phase for (a) $[0/90]_{3s}$ specimen, (b)$[90/0]_{3s}$ specimen, (c) $[\pm 45]_{3s}$ specimen, (d) $[0/0/0/45/-45/0]_S$ specimen, (e) $[0/45/-45/0/0/0]_S$ specimen.

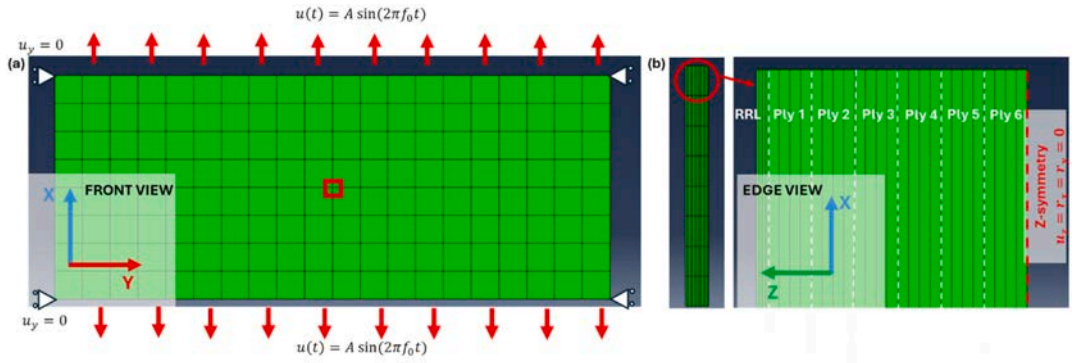

Fig. 3. (a) Longitudinal and (b) through thickness representation of the FEA simulation in Abaqus.

Table 5
Properties for simulation of matt black paint [40].

Property	Matt black paint
Thermal conductivity k (W m K^{-1})	0.7
Density (kg m^{-3})	1153
Specific heat C_p (J kg^{-1} K^{-1})	1500

neglected. The simulated temperature variation across the surface of the model is uniform. However, there are discrepancies towards the edges, so values for all the models were taken from a node in the centre of the specimen, marked in red in Fig. 3.

The loading and constraints are shown in Fig. 3; extension was permitted in the x-direction, i.e. in the loading direction, whilst constraints were applied at the traction free edges. The loading was defined using the strains obtained experimentally from the DIC. All the tests were carried out in load control, with the target loads given in Table 4, but because of inadequacies in the test machine control, particularly for larger displacements and loading frequencies, the actual applied strain was different for each of the 72 tests listed in Table 4; for completeness the spatially averaged strains are provided for each test, at each loading frequency, in Table A1. To obtain the displacement input into the FEM model, each average strain value was converted to a displacement, using the representative length prescribed in the model as the gauge length, ℓ. Thus the displacement applied for each simulation can be expressed as a function of time, as follows:

$$\varepsilon(t)\ell = u(t) = A\sin(2\pi f_0 t) \tag{4}$$

where A is the displacement amplitude obtained from the x-direction strains (see Table A1).

Eq. (4) was applied to each of the tests detailed in Table 4, so that for each of the 72 cases the model could be cyclically loaded in an identical manner to the tests. A total of 3 loading cycles were simulated. A

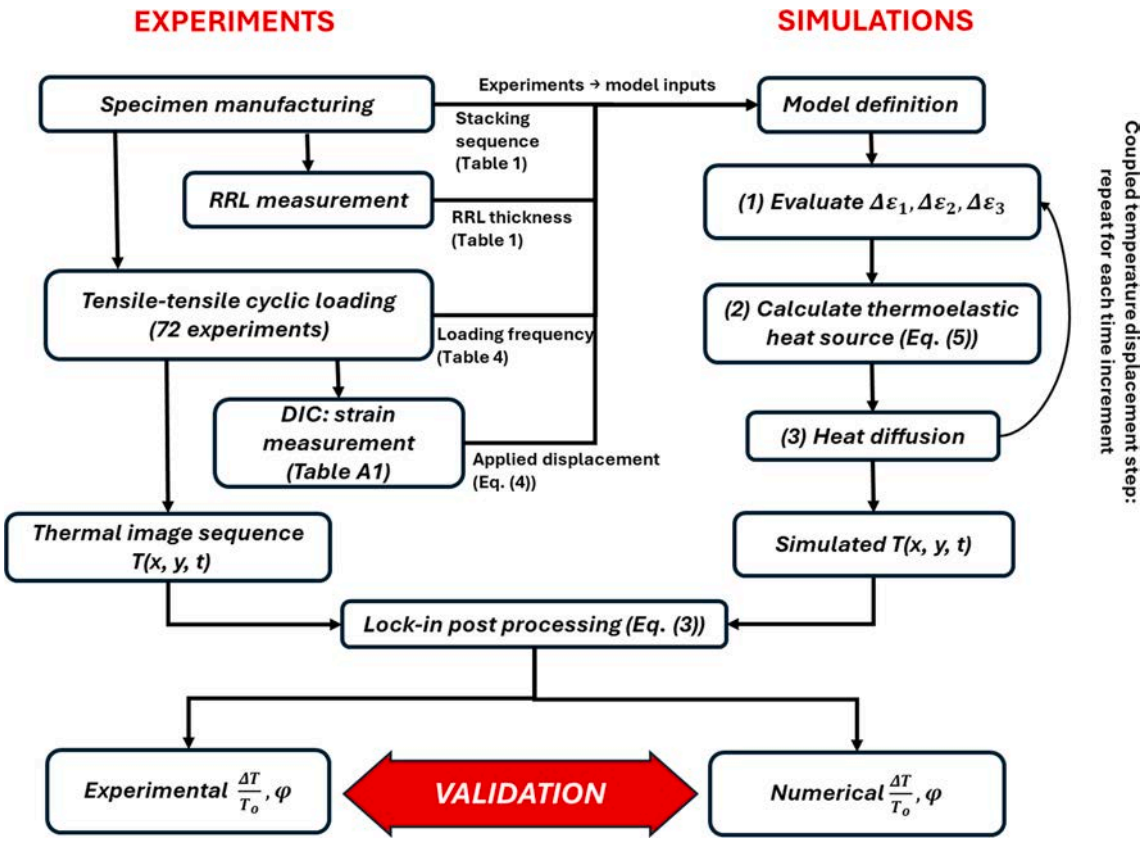

Fig. 4. Diagrammatic representation of the FEM model framework and its experimental validation.

schematic of the modelling framework is shown in Fig. 4, alongside the equivalent steps in the experimentation. Fig. 4 shows how the experimentally derived strains provide input to the model and how the experimentally obtained $\Delta T/T_0$ is used to validate the model. The modelling framework is illustrated step by step, starting with the model definition described above. A strain-based formulation [9] was implemented in a user-defined subroutine to establish the 3D thermoelastic heat source in each ply at the element level as follows:

$$\rho C_e \Delta T = T_0[(C_{11}\alpha_1 + C_{12}\alpha_2 + C_{13}\alpha_3)\Delta\varepsilon_1 + (C_{21}\alpha_1 + C_{22}\alpha_2 + C_{23}\alpha_3)\Delta\varepsilon_2 + (C_{31}\alpha_1 + C_{32}\alpha_2 + C_{33}\alpha_3)\Delta\varepsilon_3\,] \quad (5)$$

where $\Delta\varepsilon_i$ are the peak-to-peak strains, α_j are the coefficients of thermal expansion in the principal material directions and C_{ij} are the stiffness tensor components; all expressed in contracted notation.

Fig. 4 shows how the thermoelastic heat source is determined incrementally at each time step of the analysis, thereby incorporating heat diffusion, $k\nabla^2 T$ term in the numerical implementation, enabled by the spatial and temporal finite element discretisation. Utilising Eq. (5) means thermal diffusion is accounted for both in-plane and through the laminate thickness. However each ply is treated as a homogeneous anisotropic layer so interactions between the fibre and the resin are not modelled. The model does not include intrinsic dissipation or the internal energy terms given in Eq. (2) but it does include $\dot{q}_s$, i.e. convective interactions with the surroundings. A more detailed description of the model implementation is given in [9].

Fig. 4 shows that the derived temperature changes from the model are processed using the same lock-in procedure as the experiments. To ensure stability a full load cycle is required [9], so the temperature variation from the first cycle is excluded. The final step in Fig. 4 is the validation which is described in the next section of the paper.

6. Model validation

The experimental results presented in section 4 were used as the basis for validating the FEM-model framework. As the RRL was modelled as a layer of uniform thickness it was considered sufficient to conduct the validation using the spatial average of $\Delta T/T_0$ (as described above) and phase derived from the experimental data. Agreement between experimental and numerical results was deemed satisfactory if the simulated values fell within the standard deviation of the experimental data. As mentioned earlier, two sets of CTEs provided in [13] are employed ($CTEs_1$ and $CTEs_2$). Simulations were conducted both with and without the 10 μm paint layer for $CTEs_1$ while when $CTEs_2$ are employed only the configurations with paint were considered. The effect of a ± 20% variation in both the density and specific heat values given in Table 5 was investigated. This had little effect on the thermoelastic response at low frequencies and provided only a 10% increase/decrease at higher loading frequencies for a 10 μm paint thickness. The comparisons between the FEM model output and the spatial average from the experiments is presented in the following sections. For each lay-up, the thermoelastic response and the phase is plotted against loading frequency for four cases:

- The spatial average and standard deviation of the experimental data, is plotted in red;
- The FEM model results without the inclusion of the paint layer, using $CTEs_1$, are plotted in blue;
- The FEM model results with the paint, using $CTEs_1$, are plotted in green;
- The FEM model results with the paint, using $CTEs_2$, are plotted in yellow.

6.1. Cross ply specimens

Fig. 5 (a) and (b) show $\Delta T/T_0$ and phase for the $[0/90]_{3s}$ specimen and Fig. 5 (c) and (d) show $\Delta T/T_0$ and phase for the $[90/0]_{3s}$ specimen. It is evident that the FEM model successfully captures the response of both the cross ply specimens, showing good agreement with the trend of the experimental data across the entire frequency range, for both the CTEs pairs considered. The inclusion of the 10 μm paint layer in the simulations, produces $\Delta T/T_0$ values that match the experimental results, with a slightly better agreement when $CTEs_2$ are employed in the FEM model. As mentioned above, the phase plots for both the cross-ply laminates show a response that is close to 180°. This is because a transverse stress is generated in the surface ply as a result of the different Poisson's ratios of the 0° and 90° plies, which is sufficient to provide a positive ΔT. Recalling Eq. (1), even for materials with negative CTE, if $|\alpha_1\Delta\sigma_1| < |\alpha_2\Delta\sigma_2|$, the overall thermoelastic response will be 180° out of phase with the applied load. Hence, the maximum thermoelastic response in the 0° and 90° plies in the load cycle are in-phase with each other, significantly reducing the thermal gradient between the plies, which favours the onset of adiabatic behaviour. The phase reported by the model for $[0/90]_{3s}$ specimen only agrees with the experiment at the lowest loading frequency, whereas the phase for the $[90/0]_{3s}$ specimen is captured by the FEM model. The reason for the small difference in phase shown in Fig. 5 (b) may be attributed to variations in thickness of the surface RRL caused by the distribution of fibres in the resin that are not captured by the model, with in plane conduction occurring at the lower loading frequencies between the fibres and the resin. The variation in RRL is evidenced in Fig. 1 (a) by the marked changes in the response that correspond to the 0° surface ply fibres, indicating that there are regions on the specimen surface that are dominated by either the fibre or resin response. In contrast the $[90/0]_{3s}$ specimen has a much more uniform response (see Fig. 1(b)) and consequently smaller standard deviations in the experimental results shown in Fig. 5 (c).

6.2. Angle ply specimen

A comparison of the experimental and numerical results for the $[\pm 45]_{3S}$ specimen is provided in Fig. 6 (a) and (b). An offset is apparent between the experimental and numerical derived $\Delta T/T_0$ values. Unlike the cross ply specimens, where an excellent agreement was found when simulations included the paint layer, in this case the best agreement is with the unpainted case. Furthermore, in the phase plot a significant departure occurs between the experimental values and the simulation at 15 Hz. As the same material properties yielded accurate predictions for $[0/90]_{3S}$ and $[90/0]_{3S}$ specimens, the differences cannot be attributed to inaccurate material input to the FEM model. Instead, two plausible explanations emerge: i) the onset of viscoelasticity, and likely to occur at higher loading frequencies, particularly with resin dominated behaviour, or ii) the presence of higher order thermoelastic effects [16] as described in section 2, neither of which are accounted for in the FEM model.

Studies conducted by Dunn et al. [41] demonstrated that second-order thermoelastic effects can arise in ± 45° CFRP laminates. Specifically, they investigated the influence of mean strain on the thermoelastic response of various CFRP configurations, finding that such effects were significant only for ± 45° specimens. Their results revealed a linear dependence of the first harmonic of the thermoelastic response on mean strain. The mean stress that was applied to the $[\pm 45]_{3S}$ specimen is provided in Table 4, which equates to a mean strain of approximately 2800 με. According to [41] this could lead to an increase in $\Delta T/T_0$ of up to 30–40%. However, since the exact material system used in their study is uncertain, a direct numerical match cannot be established. Nonetheless, the order of magnitude of the mismatch observed in the present study aligns with the findings in [41], strongly indicating that higher-order effects could be the source of the difference and should not be neglected when analysing ± 45° specimens. To investigate further and

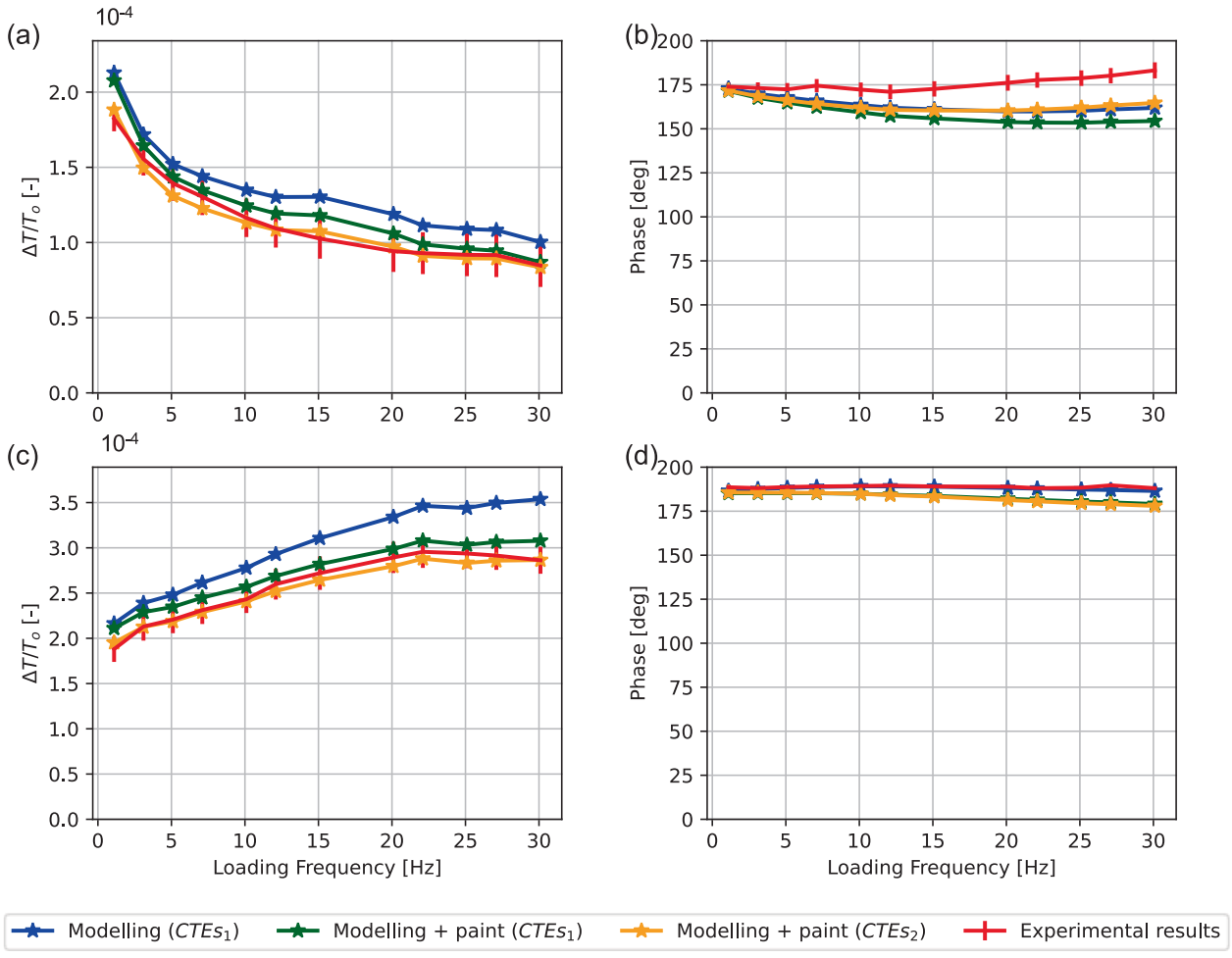

Fig. 5. (a) $\frac{\Delta T}{T_0}$ and (b) phase vs loading frequency for $[0/90]_{3s}$ specimen (c) $\frac{\Delta T}{T_0}$ and (d) phase vs loading frequency for $[90/0]_{3s}$ specimen.

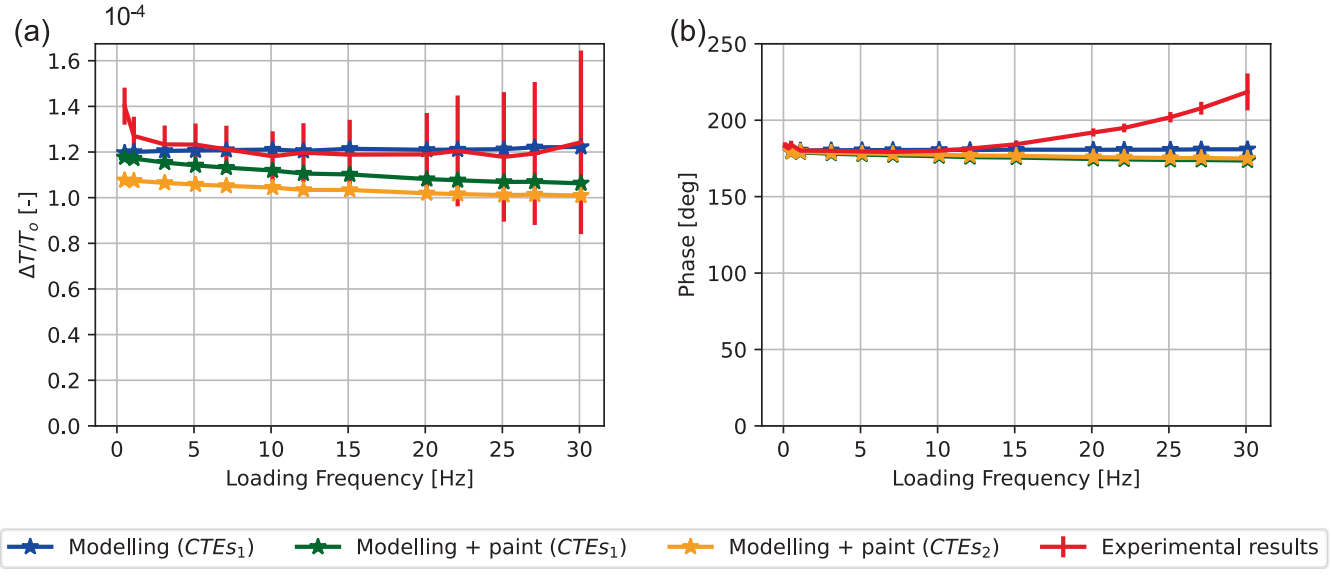

Fig. 6. (a) $\frac{\Delta T}{T_0}$ and (b) phase variation with loading frequency for $[\pm 45]_{3s}$ specimen.

correct the numerical results accordingly, a series of additional tests were performed with varying mean stress, while keeping the cyclic amplitude fixed at 46.3 MPa. The mean load was incremented from 61.72 MPa to 92.6 MPa in 7.7 MPa steps. Tests were conducted at three frequencies (1.1 Hz, 10.1 Hz, and 20.1 Hz), providing a total of 15 data points. The results of a linear regression of the spatial average of $\Delta T/T_0$ for all three loading frequencies are reported in Fig. 7 (a). Hence, a correction factor was determined by taking the ratio of the predicted

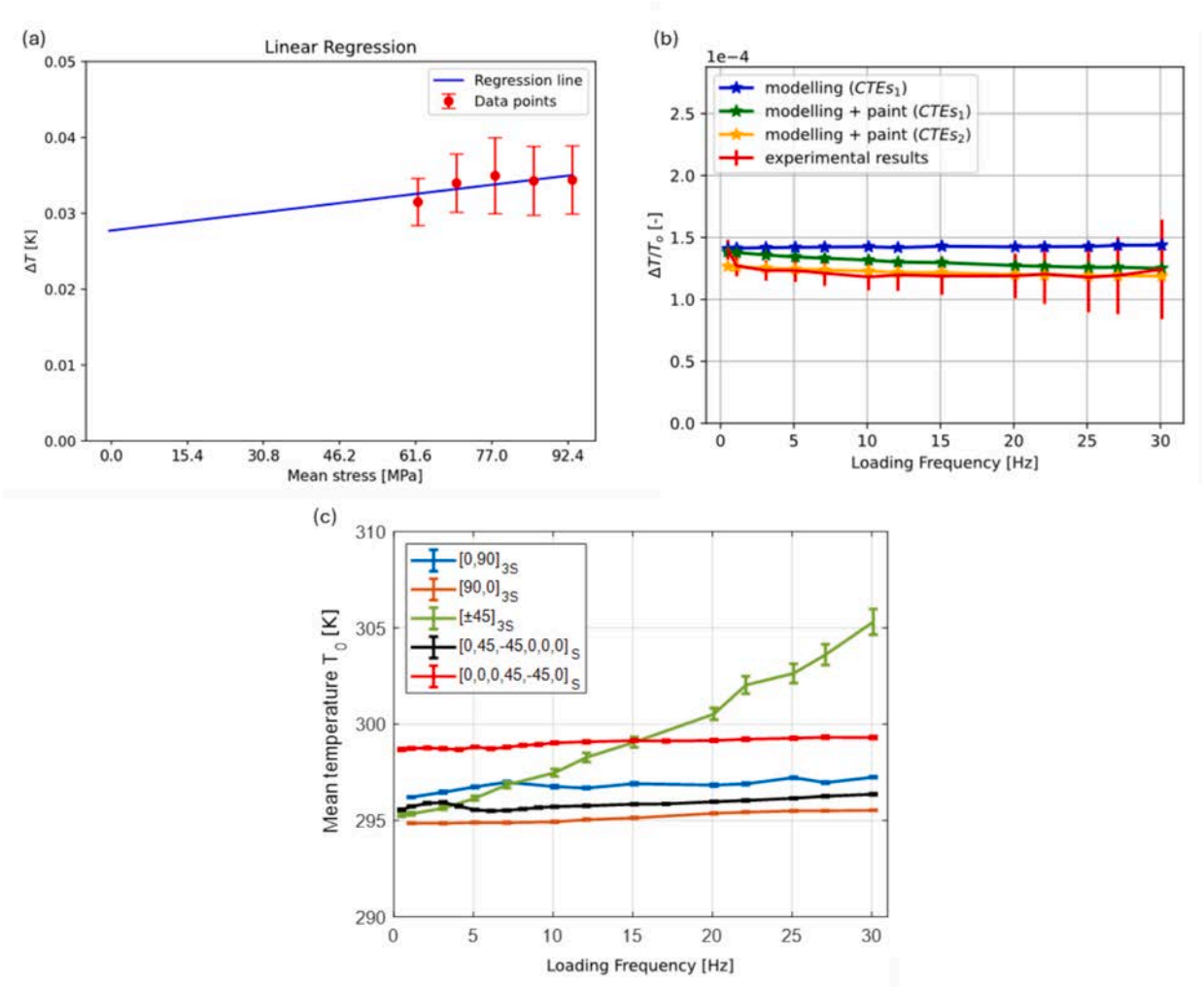

Fig. 7. (a) results of the linear regression of the thermoelastic response vs the applied mean load, (b) corrected results for the $[\pm 45]_{3s}$ specimen, (c) change in T_0 with loading frequency for all test specimen configurations.

thermoelastic response at 61.72 MPa mean stress to the extrapolated value at 0 mean stress:

$$\frac{\Delta T_{MS=61.72}}{\Delta T_{MS=0}} = \frac{0.0326}{0.0277} = 1.177 \tag{6}$$

Fig. 7 (b) shows the agreement between the FEM model and the experimental data is significantly improved with the inclusion of the correction factor given by Eq. (6). It is important to note for laminates with arbitrary ply orientations, a correction factor may be required at each loading frequency.

While higher-order effects provide a plausible explanation for the magnitude discrepancy, the observed phase shift (see Fig. 6 (b)) at higher frequencies suggests that viscoelastic effects may also play a role. Specifically, at frequencies above 15 Hz, the increasing thermoelastic phase delay indicates a progressive deviation from purely elastic behaviour. As ΔT is directly related to volumetric strain, any delay in strain evolution, such as that caused by viscoelastic behaviour, would produce a corresponding phase shift, as well as an increase in the mean temperature of the sample. The $[\pm 45]_{3S}$ specimen is shear dominated, and this causes the viscoelastic heating, i.e. straining the specimen more means there is more shearing. Hence the application of larger loads result in increased strain rates across all frequencies, thereby amplifying possible viscoelastic heating and changes in the thermoelastic response with the mean stress [16,41]. Fig. 7 (c) shows the spatially averaged T_0 values plotted against frequency, which shows T_0 increases only slightly for all except the $[\pm 45]_{3S}$ specimen. The small increases with mean stress could be attributed to intrinsic dissipation. However the marked increase in T_0 of about 10 K for the $[\pm 45]_{3S}$ specimen, can only be attributed to the shear-dominated behaviour causing heat generation. Interestingly tests on identical $[\pm 45]_{3S}$ specimens at a lower load [7], did not exhibit evidence of viscoelastic behaviour. These findings highlight the need to extend the current modelling framework to include viscoelastic behaviour, higher order thermoelastic effects and intrinsic dissipation, which is not trivial. The higher order thermoelastic formulations available in the open literature are based on simplified assumptions, such as isotropic material behaviour and simple uniaxial stress states [16,41]. Furthermore, higher order thermoelastic effects depend on the variation of elastic constants with temperature, which are not well-characterised and readily available for CFRP materials.

6.3. Multidirectional specimens

Fig. 8 (a) shows a comparison of the $\Delta T/T_0$ from the FEM model and the experiment for the $[0/0/0/45/-45/0]_s$ specimen. In the initial part of the curve, at a very low loading frequency, the response is mostly homogenised across the thickness of the laminate. At medium loading frequencies (2 to 6 Hz), the three adjacent 0° plies near the surface act as a barrier to heat transfer, preventing heat from diffusing into the ± 45° plies within the laminate. As a result, the surface plies dominate the response, leading to an increase in $\Delta T/T_0$ for the initial part of frequency

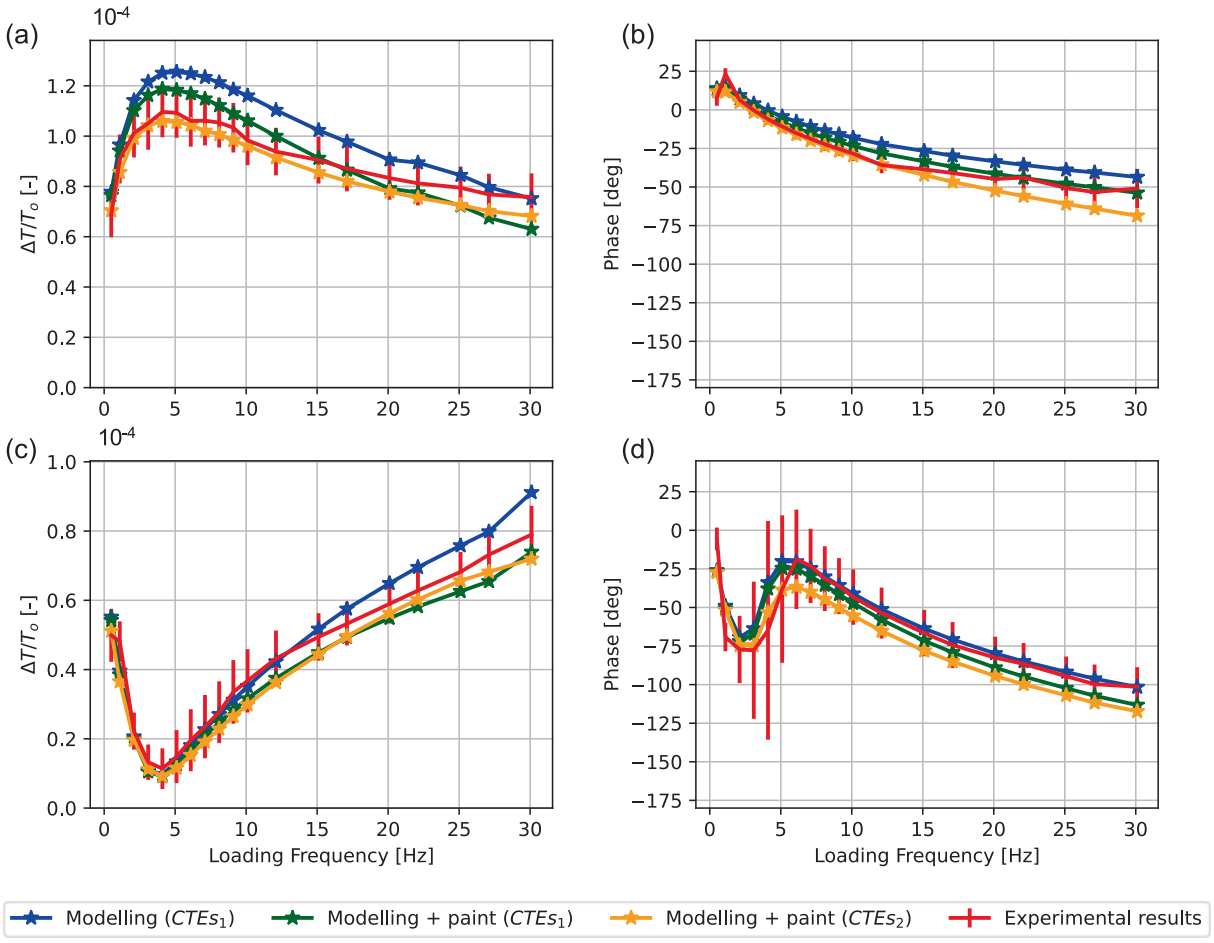

Fig. 8. (a) $\frac{\Delta T}{T_0}$ and (b) phase variation with loading frequency for $[0/0/0/45/\text{-}45/0]_s$. (c) $\frac{\Delta T}{T_0}$ and (d) phase variation with loading frequency for $[0/45/\text{-}45/0/0/0]_s$.

range. However, as the frequency increases beyond 5 Hz, heat transfer reduces and the influence of the RRL becomes more pronounced. The RRL has a positive CTE, which favours a response that is out of phase with load cycle, in contrast the negative CTE of the 0° plies favours a response that is in phase with the load cycle. As the loading frequency increases, the RRL generates a reduction in the overall thermoelastic response at the surface. The numerical model accurately captures the trend of the experimental results, including the frequency at which the change in the heat transfer direction occurs. Hence, the predictive capability of the FEM model is further confirmed in the presence of a thick RRL. To aid interpretation, the change in $\Delta T/T_0$ ply by ply is discussed in detail in the following section. A comparison of the phase shift from the FEM model and the experiments with loading frequency for the $[0/0/0/45/\text{-}45/0]_s$ specimen is provided in Fig. 8 (b). At low frequencies, the phase is close to 0°, indicating a dominance of the 0° plies. As the frequency increases, the phase gradually shifts, reflecting a transition to a resin-dominated response, caused by the thick RRL. This is supported by the results of [13], where identical stacking sequences were used in specimens made from IM7/8552, with a much thinner RRL of 8 μm. Hence, in [13] the reported phase values were much closer to zero.

Fig. 8 (c) shows a comparison of the experimental and FEM model $\Delta T/T_0$ values for the $[0/45/\text{-}45/0/0/0]_s$ specimen, confirming that the model can capture the complex heat transfer characteristics. The response of the $[0/45/\text{-}45/0/0/0]_s$ specimen contrasts with the $[0/0/45/\text{-}45/0]_s$ specimen as a result of the interplay between the surface 0° ply, the subsurface ± 45° plies, and the RRL. At low frequencies, significant heat transfer with the subsurface ± 45° plies takes place, reducing the contribution of the surface 0° ply to the thermoelastic response. Since the RRL thickness is significant (~18 μm), heat is transferred away from the surface 0° ply up to ~ 4 Hz, where the smallest response occurs. As the loading frequency increases, heat transfer diminishes and the response increases. The phase plot shown in Fig. 8 (d) supports the explanation, initially, the phase drops to a minimum, suggesting a reduction in the influence of the 0° ply. However, at higher frequencies, the phase continues to decrease indicating a regime where the response is dominated by the RRL, even though adiabatic conditions are not reached.

It is clear that in all cases, apart from the ± 45° specimen, the numerical model successfully replicates both the $\Delta T/T_0$ and the phase trends, confirming its ability to describe the complex interplay between heat transfer mechanisms and material properties. The RRL clearly has a strong effect on both $\Delta T/T_0$ and the phase, including the RRL in the model is essential to interpret the complex heat transfer conditions it generates, that are clearly dependent on the subsurface lay-up. One interesting outcome is that, even with a thick RRL (e.g. 38 μm) a general strain witness scenario approach seems unlikely for CFRP laminates, which is explored further in the next sections of the paper. The inclusion of the paint layer in the model is justified as this significantly improves the agreement with experimental results.

7. Simulation of subsurface response

A key advantage of the FEM model is that it can predict the response for each ply in the laminate, and hence aid the understanding of heat transfer. Additionally, when using TSA to assess subsurface damage the FEM model can aid in identifying a loading frequency to probe damage evolving in certain plies. Hence, the modelling framework is used to

obtain $\Delta T/T_0$ and the phase ply-by-ply. The $[0/45/\text{-}45/0/0/0]_s$ specimen was selected as a representative case, because it has an intermediate RRL thickness and the off-axis plies close to the surface generate a complex response. Simulations were conducted both without (Fig. 9 (a, c, e, g)) and with (Fig. 9 (b, d, f, h)) the RRL, allowing for a direct comparison of the through-thickness thermoelastic response. The plots present the through-thickness ply-by-ply $\Delta T/T_0$ (blue curve) and phase (red curve) extracted at 4 loading frequencies, where x = 0 denotes the mid-plane of the laminate. To allow a visualisation without any heat transfer effects, i.e. according to Equation (1), Fig. 9 (a) and (b) gives the results for an idealised adiabatic condition generated at a loading frequency of 1 MHz. Fig. 9 (c) and (d) shows the results for 0.5 Hz, Fig. 9 (e) and (f) for 7.1 Hz and Fig. 9 (g) and (h) for 30.1 Hz. Only results from the simulations without the paint layer are reported, as a detailed parametric study on the influence of the paint is presented separately in Section 8.1.

Fig. 9 (a) and (b) show the adiabatic case, where the response from each ply and the RRL are fully isolated. It is very clear that due to the negative α_1 of the 0° ply, the thermoelastic response results in a phase value of zero and that the response from ± 45° plies and RRL provides a phase value of 180°. The idealised response from the RRL is much greater than that of the 0° ply, meaning that for non-adiabatic conditions heat transfer would occur from the RRL into surface ply. The heat transfer is amplified, because the maximum temperature in the load cycle in the 0° ply, occurs when the RRL generates its minimum temperature (i.e. 180° out of phase). As expected, the + 45° and −45° plies generate an identical $\Delta T/T_0$, but with a smaller value than the 0° ply, meaning that for non-adiabatic conditions heat will be transferred from the 0° plies into the ± 45° plies. Hence, here the response from the RRL is the greatest. Fig. 9 (a) and (b) provide a very useful starting point in understanding the heat transfer paths that occur at the lower loading frequencies and aids in interpretation of the role of the RRL in TSA of CFRP composites.

For the lowest frequency of 0.5 Hz (Fig. 9 (c) and (d)), it is apparent that the thermoelastic response from each ply is similar, indicating a large degree of homogenisation resulting from significant heat transfer and a global laminate response. The phase differences between plies indicate variations in the timing of peak temperature changes, and at a low loading frequency these are small, providing further evidence for the homogenisation. Interestingly the phase is close to zero indicating the dominance of the 0° plies. The concept of homogenisation is a significant finding in the context of TSA on large structures, where only very low loading frequencies can be applied. It is also interesting that the RRL has little effect on the surface response, which at this frequency is much less than the adiabatic case. However, the response is sufficient to make measurements, so adopting the calibration procedure described in [19] to evaluate stresses would be possible. Moreover, the results in Fig. 9 (c) and (d) provide an explanation for the findings of [19], where it was shown for tests on CFRP sandwich panels at low frequency, the most effective type of calibration was based on the global laminate response.

In Fig. 9 (e) and (f) it can be seen that at a loading frequency of 7.1 Hz the response from each ply is different, since the thermal diffusion length decreases. Here the inclusion of the RRL results in a significant reduction in the thermoelastic surface response, because heat is being transferred from the RRL into the 0° ply. Heat is also transferred from the 0° plies into the ± 45° plies, with the response from the 0° plies being significantly less than the adiabatic case.

In Fig. 9 (g) and (h) it can be seen that with a 30.1 Hz loading frequency, the response from each ply becomes more isolated and tends toward the adiabatic case. In fact without the RRL the surface response is practically identical to the adiabatic case, even though heat is still being transferred from the 0° plies into the ± 45° plies. There is an increase in the surface response with the inclusion of the RRL, even though heat is transferred from the RRL into the 0° ply. It is very clear that the negative CTE of the 0° ply plays a critical role in the evolution of the surface response. This is evident in the phase value shown in Fig. 9 (h), which even at 30 Hz is not close to 180°, indicating the adiabatic conditions shown in Fig. 9 (b) have not been achieved. Hence, a detailed parametric study of the effect of the RRL thickness on the surface response is presented in the next section of the paper. It is clear that the RRL alters the surface response, but it has little influence on the deeper plies, which means at the lower loading frequencies there is a potential for TSA to probe subsurface defects.

8. Parametric study of the influence of the RRL and paint coating

The numerical results presented in Figs. 5, 6, 7, 8 and 9 have confirmed that both the RRL and paint layer can significantly influence the measured thermoelastic response. The analysis in section 7 demonstrated that adiabatic behaviour is only achieved if the phase is either 180°, indicating a negative $\Delta T/T_0$, or is 0°, indicating a positive $\Delta T/T_0$. Moreover, even if $\Delta T/T_0$ appears to be asymptotic as the loading frequency changes, this alone is not an indication of an adiabatic thermoelastic response. To systematically explore this premise, a parametric study was devised, where the thicknesses of both the RRL and the paint coating were evaluated, to investigate their impact on the thermoelastic response and phase shift. Both multidirectional laminates ($[0/0/0/45/\text{-}45/0]_s$ and $[0/45/\text{-}45/0/0/0]_s$) were selected for this analysis and two types of simulation were performed using the FEM model:

1. The paint thickness was varied from 0 to 50 μm, considering a RRL of 10 μm, since it represents a realistic thickness often encountered in practical applications.
2. The RRL thickness was varied from 0 to 125 μm (i.e., the same thickness as a ply and regarded as the largest feasible thickness to be generated during typical manufacturing processes), without the inclusion of the paint layer coating.

8.1. Effect of paint layer thickness

Fig. 10 (a) to (d) show $\Delta T/T_0$ and the phase plotted against loading frequency for both multidirectional laminates for the range of paint coating thicknesses. The "thermal lag" [39] or damping effects of the paint layer are evident with a significant reduction of $\Delta T/T_0$ with both values of paint thickness. There is also a clear reduction in response with loading frequency accompanied by progressive phase delay, known as "thermal drag down" [39] caused by the reduction in thermal diffusion length as the rate of change of the temperature increases. These findings confirm earlier work that demonstrates experimentally or analytically that the coating should be as thin as possible. Moreover, a uniform paint coating is essential as regions of excessively thick coatings can result in a significant underestimation of the thermoelastic response. As CFRP materials are characterised by a low thermoelastic response in the direction of the fibres, the effects of the paint on both configurations are marked with a 50% reduction in response at around 20 Hz. The results suggest that low loading frequencies should always be used to minimise the effect of the paint and justifies the use of unpainted specimens in [13] for estimating the CTEs. However, it is important to note that paint layers are not load bearing, so their presence does not affect the through thickness heat transfer. Instead, the paint introduces a thermal damping, which scales $\Delta T/T_0$, whilst introducing a small phase shift. It is also important to note that when DIC is used simultaneously with TSA, as was the case for the validation studies described above, great care should be taken in the application of the speckle pattern so as not to introduce localised thicker regions of paint.

8.2. Effect of RRL thickness

Fig. 11 (a) and (b) show the effect of RRL thickness with loading

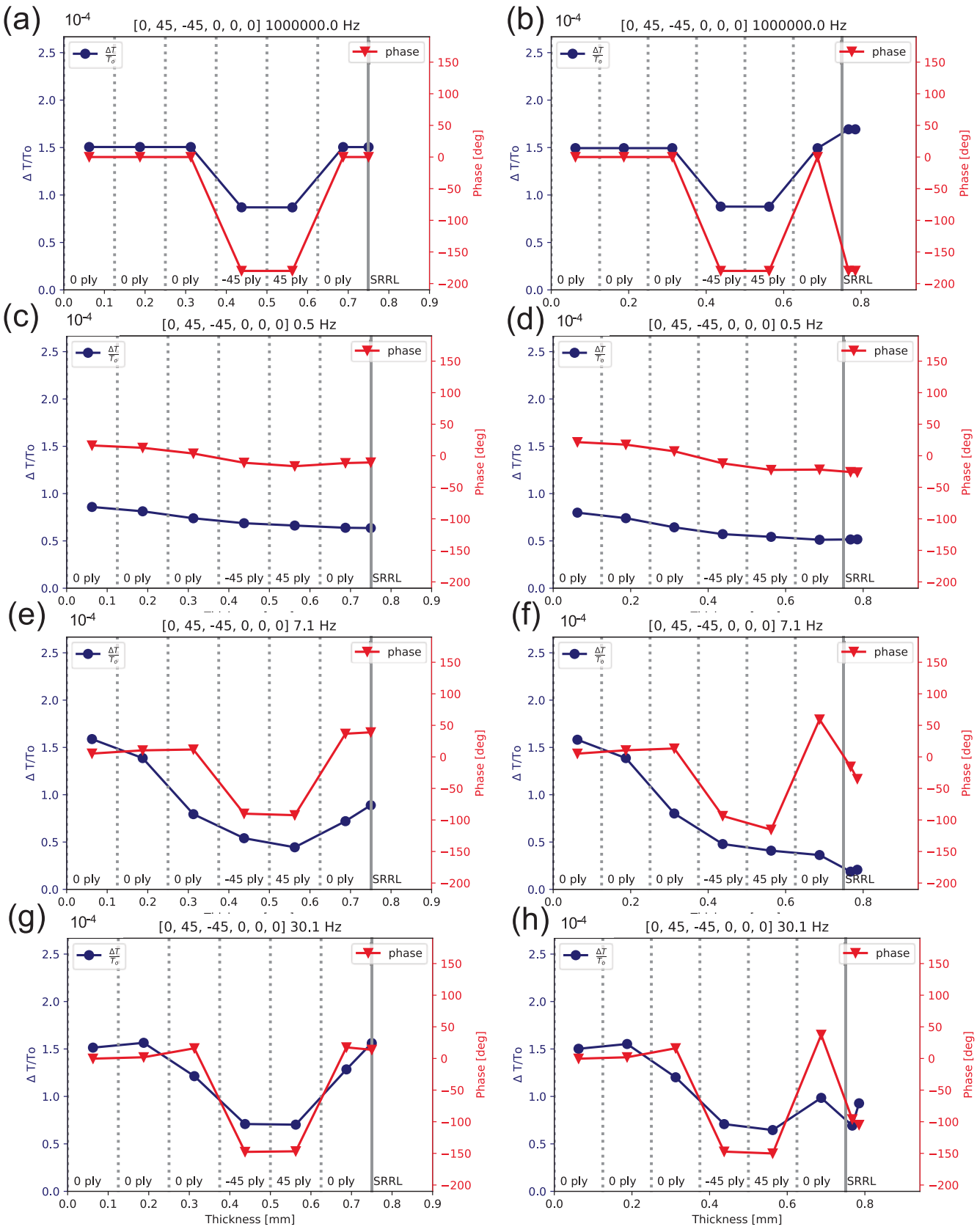

Fig. 9. Through thickness temperature profile for the $[0/45/-45/0/0/0]_s$ specimen with and without surface resin rich layer. Four loading frequencies: (a, b) adiabatic (1000000 Hz), (c, d) 0.5 Hz, (e, f), 7.1 Hz and (g, h) 30.1 Hz. Simulations are repeated without RRL (left, a, c, e, g) and with RRL (right, b, d, f, h).

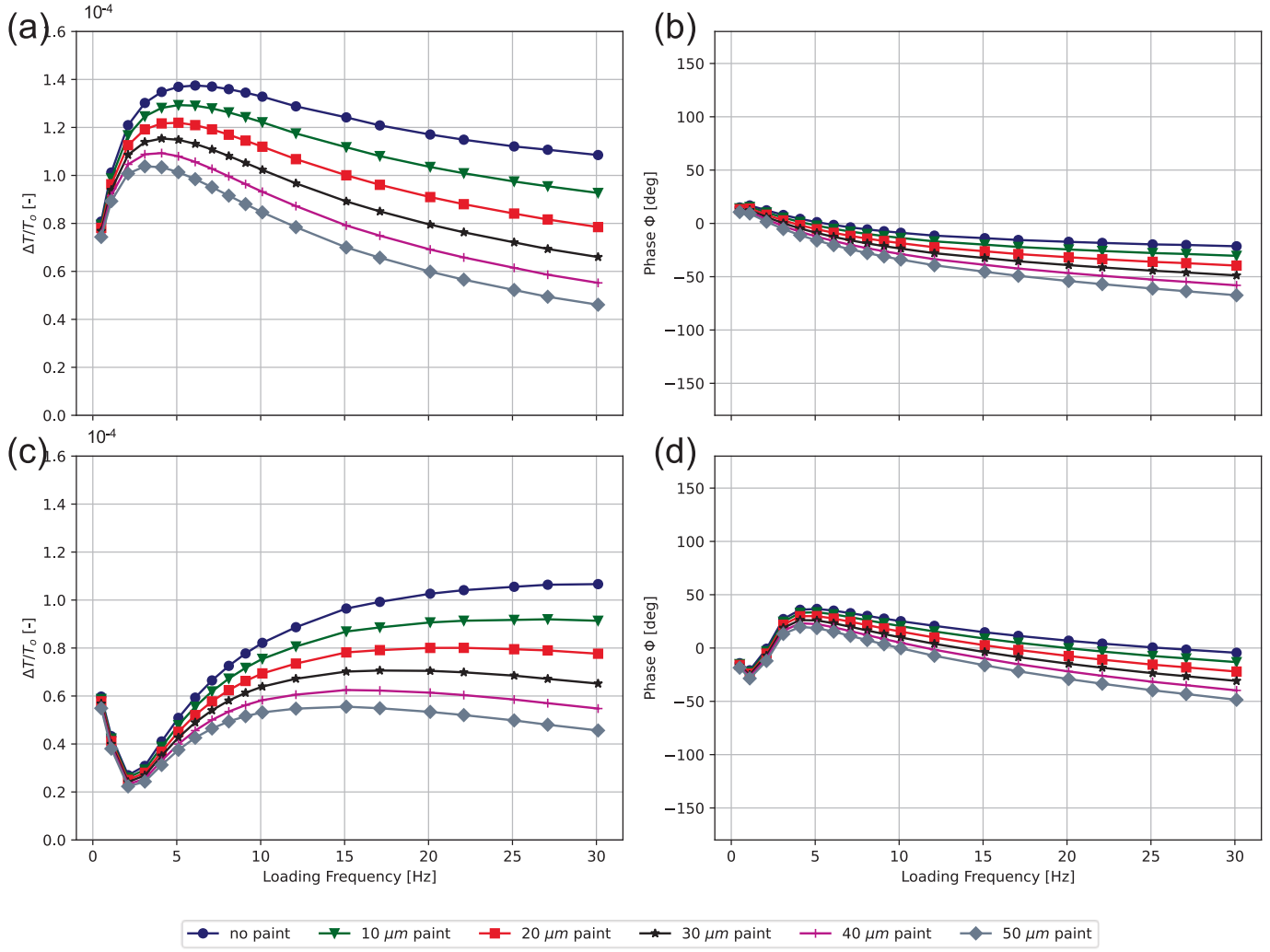

Fig. 10. (a) $\frac{\Delta T}{T_0}$ and (b) phase variation with loading frequency for the $[0/0/0/45/\text{-}45/0]_s$ case and (c) $\frac{\Delta T}{T_0}$ and (d) phase variation with loading frequency for the $[0/45/\text{-}45/0/0/0]_s$ case with paint thickness varying from 0 to 50 μm.

frequency on $\Delta T/T_0$ and phase for the $[0/0/0/45/\text{-}45/0]_s$ cases. Likewise, Fig. 11 (c) and (d) show the effect of RRL thickness with loading frequency on $\Delta T/T_0$ and phase for the $[0/45/\text{-}45/0/0/0]_s$ cases. Included in Fig. 11 (a) and (c) are two dotted lines which represent two of the models described in [7]; one is the calculated response from the isolated "surface ply" and the other when the response is only from the resin, i.e. "strain witness". It is clear that changes in RRL can significantly modify the thermoelastic response at the surface, in particular, it appears to control the frequency at which the peaks and troughs in the plots of $\Delta T/T_0$ and phase occur. Interestingly, for both thinner ($\leq$20 μm) and thicker ($\geq$100 μm) $\Delta T/T_0$ becomes constant as the frequency increases, but for 40 and 80 μm $\Delta T/T_0$ continues to increase, even at 50 Hz. However, it is only for the $[0/0/0/45/\text{-}45/0]_s$ case without a RRL where $\Delta T/T_0$ converges to the calculated surface ply response as frequency increases. Importantly, even the very thick RRLs do not converge to the strain witness model, even at a frequency of 50 Hz. An examination of the phase plots in Fig. 11 (b) and (d) show that for both lay-ups only the cases where the RRL is 0 or 10 μm, the phase converges to a value close to 0° as the loading frequency increases, indicating that in these cases the response is mostly dominated by the surface ply. For RRLs thicker than 40 μm the indication is that the phase is converging to 180° as the frequency increases indicating that the RRL governs the thermoelastic response, but $\Delta T/T_0$ continues to increase, even at 50 Hz the phase only converges close to 180° for unrealistically thick RRL of 100 and 125 μm. It is clear from this that the interaction between the plies and particularly the introduction of the ± 45° plies close to the surface results in a thermoelastic response that does not fit any of the previously proposed models [7], even at loading frequencies up to 50 Hz. The indication is that heat transfer is occurring and that adiabatic conditions will not be achieved unless much greater loading frequencies are applied. Hence, it is demonstrated that the phase values extracted from the FEM model indicate when sufficiently close to adiabatic conditions have been achieved. More importantly the FEM model enables an assessment of the experimental conditions for adiabatic condition to prevail, and moreover if such an experiment is feasible.

To aid further interpretation it is useful to present the results from Fig. 11 as the in-phase (X) and out-of-phase (Y) components of the thermoelastic response i.e.:

$$X = \Delta T \times \cos(\phi); Y = \Delta T \times \sin(\phi) \tag{7}$$

where ϕ is the phase angle.

The X- and Y-components of the response are shown in Fig. 12 for both multidirectional laminates. A zero Y-component indicates adiabatic conditions and then the X-component is ΔT as given by Eq. (1). The X-component plots clearly show the response for each RRL thickness, with the $[0/0/0/45/\text{-}45/0]_s$ case increasing to a peak value and then decreasing and the $[0/45/\text{-}45/0/0/0]_s$ case reducing to a minimum value and then increasing. For the RRL thickness $\geq$ 100 μm the X-component response from both laminates is similar, with a rapid

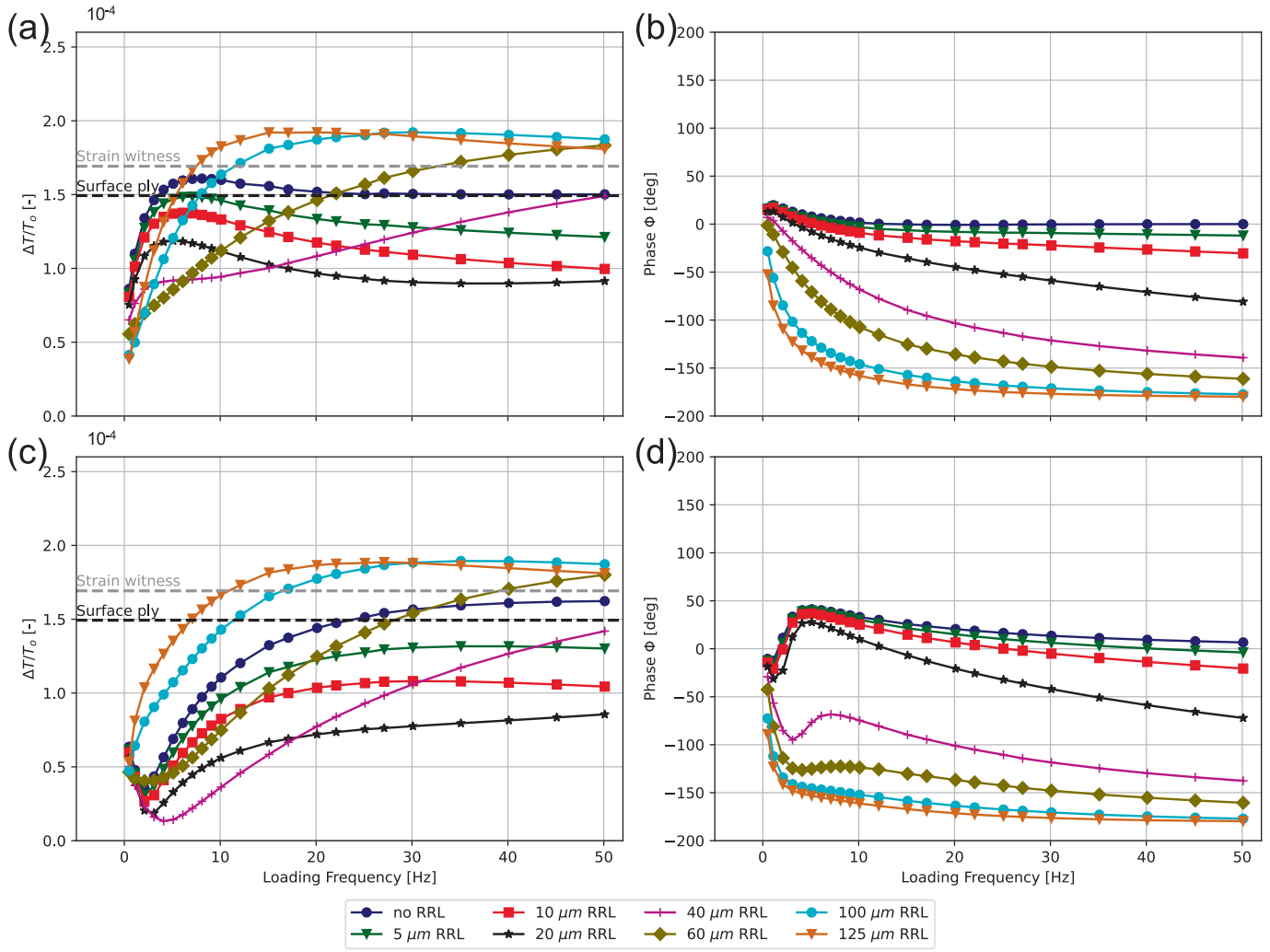

Fig. 11. (a) $\frac{\Delta T}{T_0}$ and (b) phase variation with loading frequency for the $[0/0/0/45/-45/0]_s$ case and (c) $\frac{\Delta T}{T_0}$ and (d) phase variation with loading frequency for the $[0/45/-45/0/0/0]_s$ case.

reduction in value followed by levelling out to a low value close to the strain witness response. For $[0/45/-45/0/0/0]_s$ case (Fig. 12c) the X-component response is more complex at the lower loading frequencies because of the position of the $\pm$ 45° plies closer to the surface.

The analysis of the Y-component reveals that, for the [0/0/0/45/-45/0]s laminate, adiabatic conditions are approximately attained beyond 15 Hz in the absence of an RRL, and only at 50 Hz when the RRL is 125 μm thick. In contrast, the [0/45/-45/0/0/0]s laminate does not achieve fully adiabatic conditions under any of the tested configurations, except at 50 Hz with the thickest RRL. The results confirm that the stacking sequence close to the surface of CFRP laminates, alongside the thickness of the RRL, play a crucial role in the surface thermoelastic response. Most importantly the concept of using the resin rich layer as a strain witness in CFRP to negate non-adiabatic behaviour is unlikely to be successful, for three reasons: (i) the complex interactions that occur between the resin and the plies at realistic loading frequencies and (ii) very thick RRLs are required, which would not be practical or cost effective to generate on actual structures, and (iii) in examples where out-of-plane bending occurs, the strain at the surface ply does not correspond to that of the surface of the RRL, so in instances such as monitoring damage evolution, where the degree of out of plane bending changes, even qualitative comparisons cannot be made. The most important outcome is that a FEM model, that captures the stacking sequence, ply thickness and RRL is an essential tool to interpret the thermoelastic response for a general CFRP lay-up.

9. Case studies and applications

9.1. Application #1: Simulation of a quasi-isotropic layup

A laminate with a stacking sequence of $[0/90/45/-45]_s$ was selected, since quasi-isotropic layups are typically employed for composite structures. The aim is to demonstrate the insight the FEM-model can provide, when designing a TSA-based testing campaign for a composite component. Hence, an achievable range of loading frequencies was selected (up to 10 Hz) and RRL thicknesses of 5, 10, 15, and 20 μm, typical of those found on as manufactured components, alongside a zero thickness as a baseline case. A tensile-tensile cyclic loading, with peak-to-peak strain of 2000 με was applied to a strip of dimensions 20 mm wide by 8 mm long; the ply thickness and material properties were for IM7/8552 as described in section 2. Fig. 13 (a) shows $\Delta T/T_0$ plotted against loading frequency, as with the cross ply lay-ups described in section 3 it can be seen that heat is transferred from the 90° ply into the 0° ply, because $\Delta T/T_0$ reduces with loading frequency. It is evident that the RRL layer thickness only causes a small reduction in $\Delta T/T_0$ as the response is dominated by heat transfer away from the surface. The phase plots are shown in Fig. 13 (b) and show at the lowest frequency the phase is 175° indicating that the homogenised global response is dominated by the 45° and 90° plies. As the loading frequency increases the phase values reduce, with an indication that the case without the RRL may be tending to a 0° phase value at sufficiently high loading

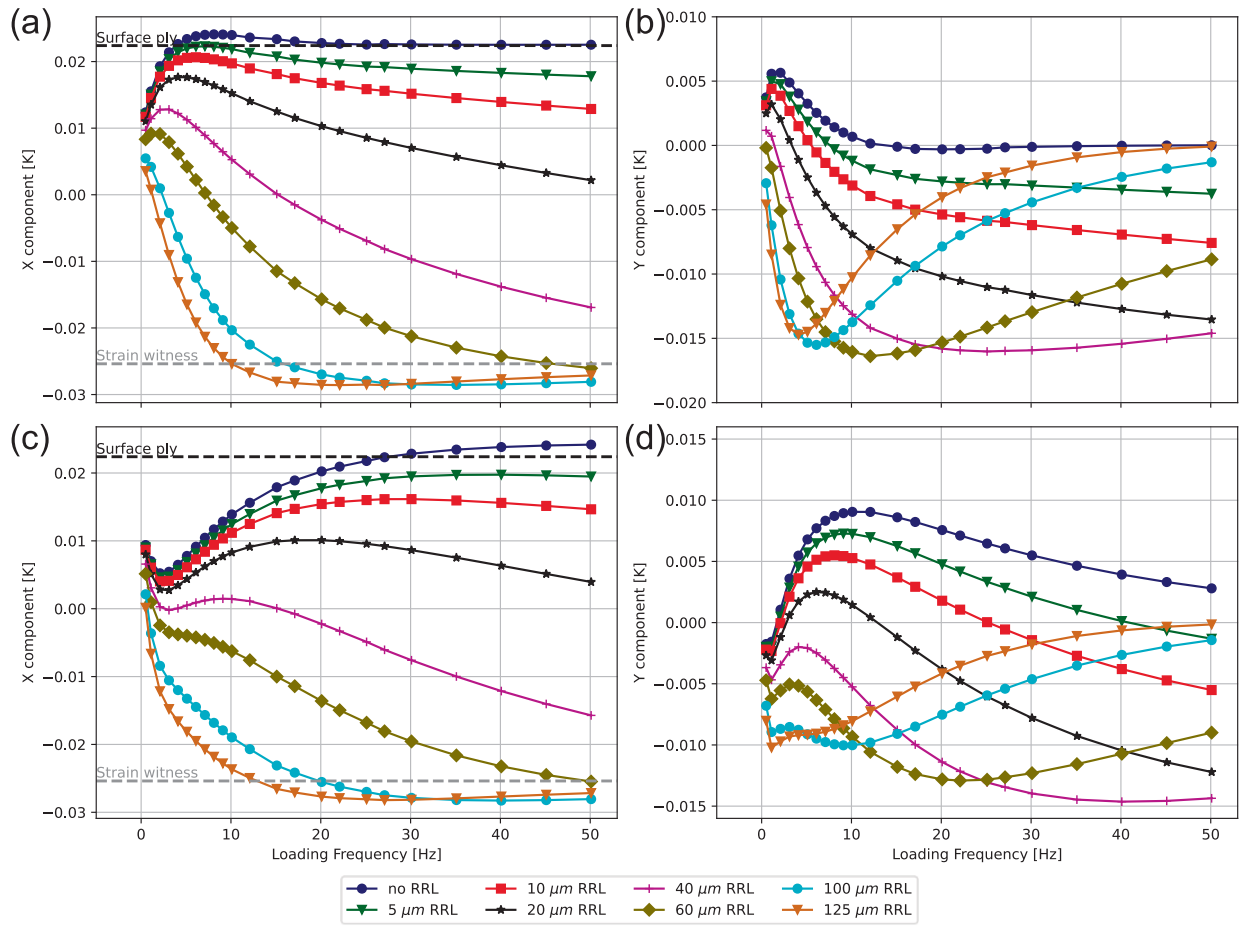

Fig. 12. (a) X (in phase) and (b) Y (out of phase) components variation with loading frequency for the $[0/0/0/45/-45/0]_s$ case and (c) X (in phase) and (d) Y (out of phase) components with loading frequency for the $[0/45/-45/0/0/0]_s$ case. RRL thickness varying from 0 to 125 μm.

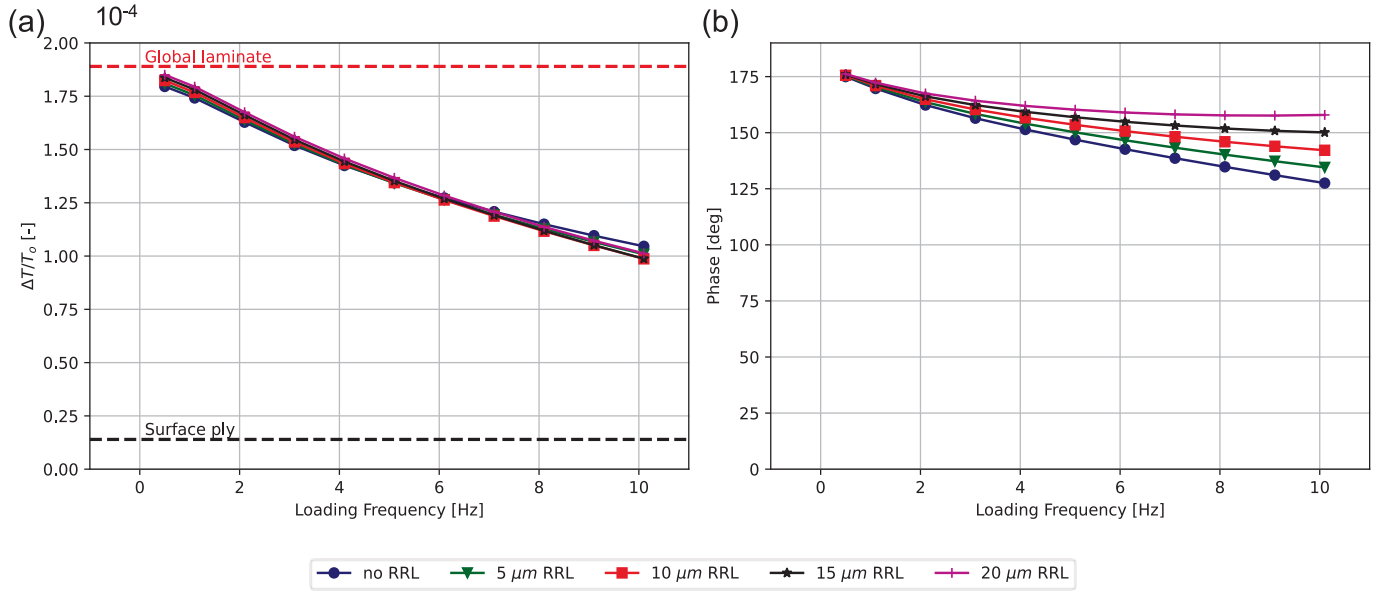

Fig. 13. (a) $\frac{\Delta T}{T_0}$, (b) phase variation with RRL thickness for a $[0/90/45/-45]_s$ demonstrator case. For reference, the $\frac{\Delta T}{T_0}$ obtained with the strain witness approach is 3.26×10^{-4}, so not included in (a).

frequencies. The RRL has a strong effect on the phase value as in each of these cases for adiabatic conditions to prevail the phase would need to be 180°. Hence, at realistic loading frequencies for CFRP structures made of thin plies, the model demonstrates that adiabatic conditions cannot be obtained. There are two options for quantitative analysis: (i) follow the approach in [19] and calibrate in terms of stress at a given

loading frequency, noting that damage will modify the heat transfer locally or (ii) conduct tests at the lowest frequency to ensure a homogenised response, that may provide a more consistent response following the introduction of damage. In both cases if the material properties are known the model can provide the calibration. The latter (ii) is yet to be demonstrated and further work is required to establish if using the homogenised response would enable quantitative stress analysis, particularly for cases where damage is evolving. However, developing a means of conducting quantitative TSA on CFRP structures at low loading frequencies would have the advantage of avoiding the onset of viscoelastic behaviour, and would align with achievable loading frequencies for large structural tests.

9.2. Application #2: C-spar demonstrator

The second application aims at assessing the predictive capabilities of the proposed modelling approach in a more realistic and challenging context using a realistic substructure in the form of a C-spar, which was to be developed as a demonstrator for the CerTest project [42]. The C-spar was not manufactured in house, instead came from a campaign of manufacturing trials where the record of the materials used had been discarded, although the lay-up was known to be $[45/-45/45/-45/45/-45/0/90/0/90/0/90]_s$. As the exact material system was unknown a micrograph of the structure, shown in Fig. 14 (a), was taken, which confirmed the stacking sequence, the ply thickness and the thickness of the resin rich layer. It can be seen the ply thicknesses are non-uniform: approximately 170 μm for the 90° plies, 303 μm for the 0° plies and 250 μm for the 45° plies. This is typical for a composite component, for instance the 90° plies at the mid plane have nested, but the cross ply interfaces are unable to nest. Rather than model each ply thickness separately, for demonstration purposes an average value of 254 μm was used in the model. The approximation of ply thickness may have an effect on the heat transfer, but it was considered acceptable as the thickness of each ply varied. The RRL was also measured as 20 μm and used in the model. Importantly, it is clear from the ply thickness the material is not IM7/8552. To demonstrate the utility of the model, as there will be many cases where the material properties are unknown, it was decided to use the IM7/8552 material properties quoted in Table 2 and both coefficients of thermal expansion pairs, $CTEs_1$ and $CTEs_2$ used previously. This will have an effect on the quantitative values extracted from the model, but the onset of adiabatic behaviour can be confirmed in a qualitative sense. The paint coating was also incorporated in the model.

For the experimental work a simple rectangular strip (200 mm × 20 mm × 6.12 mm) was extracted from the web of the C-spar. The strip was loaded in load control to the same range of loading frequency reported in Table 4, with a load of 5 ± 4.5 kN, corresponding to a peak-to-peak strain variation of 1300 με. Fig. 14 (b) compares full-field

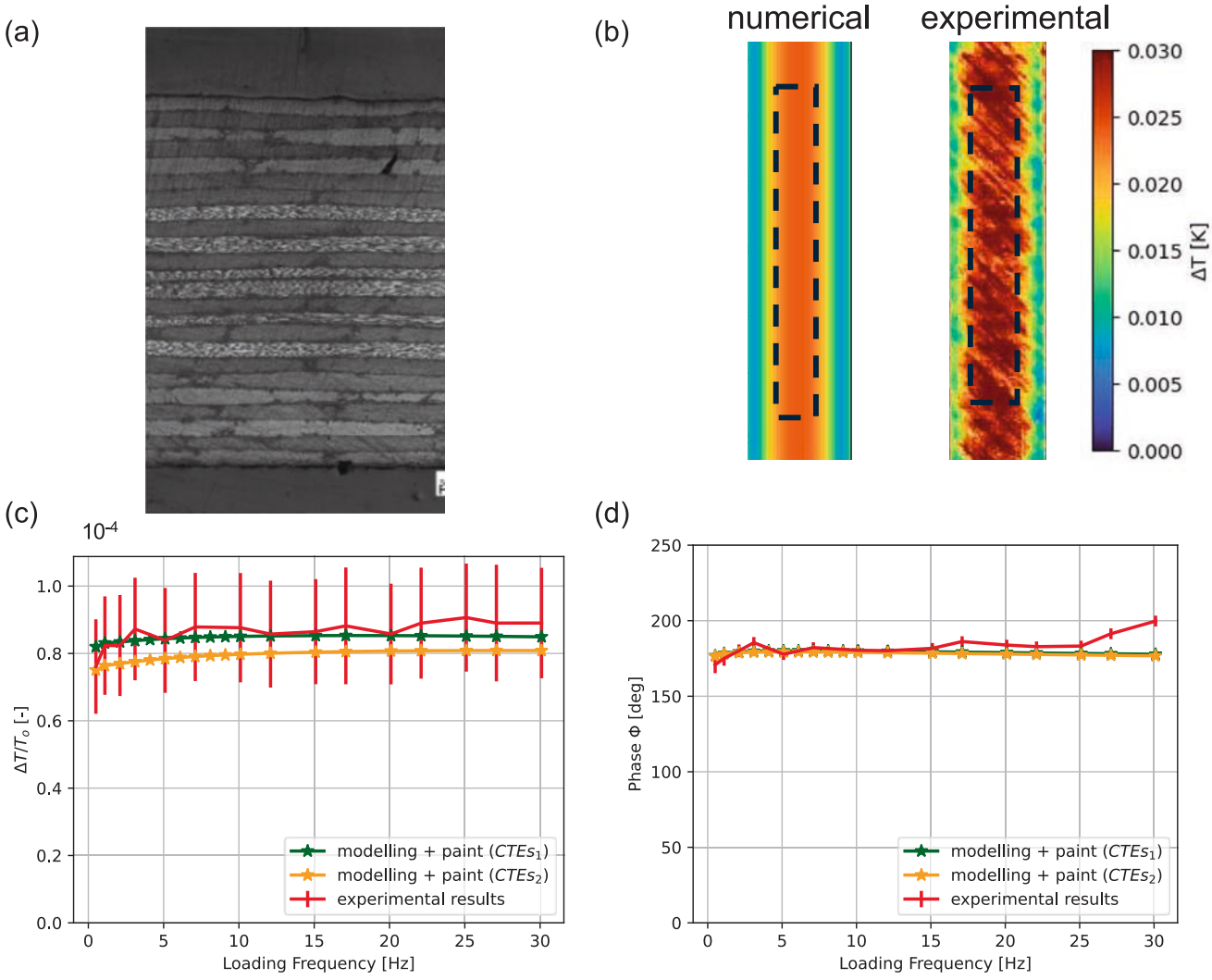

Fig. 14. (a) Micrograph of C-spar material, Comparison of FEM-model and experimental data from C-spar specimen (b) $\Delta T/T_0$ full-field maps at 10 Hz, (c) Spatial average of $\frac{\Delta T}{T_0}$ and (d) Spatial average of phase.

experimental and numerical results at 10 Hz; similar results were obtained at the other loading frequencies. The 45° surface ply is evident in the full-field experimental maps shown in Fig. 14 (b); this is not replicated by the numerical model as a homogeneous anisotropic ply material is assumed. The full-field experimental results show that $\Delta T/T_0$ is greatest in the central region, with a marked reduction towards the specimen edges, which, despite the estimated material property values and averaged ply thickness, are replicated by the FEM model. The distribution of $\Delta T/T_0$ results from the layup, and the constraining effect of the interior 90° plies causing a transverse stress on the ± 45° plies at the outer surface. The result is a distortion of the ± 45° plies and a reduced stress as the transverse normal stress decays to zero at the specimen edge. Hence, Fig. 14 (c) and (d) presents the spatial average variation of $\Delta T/T_0$ and phase with loading frequency, over the central section of the specimen (area inside dotted black box).

Fig. 14 (c) shows that $\Delta T/T_0$ becomes constant at approximately 10 Hz, indicating the onset of adiabatic conditions. Furthermore, there is very good agreement when $CTEs_1$ are used, while a small offset is observed for $CTEs_2$. The predictions fall within the experimental standard deviation, confirming that even with estimated properties and approximate laminate architecture the FEM model can provide reasonable predictions of the thermoelastic response. The standard deviations are larger than evidenced in the preceding sections, this can be attributed to the surface roughness of the specimen and surface inhomogeneities in the fibre resin distribution. For this particular stacking sequence it can be concluded that the specimen could be loaded at any frequency above 10 Hz to obtain an adiabatic response. Interestingly the phase plot of Fig. 14 (d) shows a departure from a constant phase of around 180° at 25 Hz that is not captured by the model, similar to that of Fig. 6 (b). This indicates that for this lay-up any loading frequency above 20 Hz should be avoided. The offset in the FEM model results may be attributed to the same mechanisms identified in the $[\pm 45]_{3s}$ specimen, even though the applied strains are significantly less (around 30%).

The case study has demonstrated the predictive power and robustness of the FEM model for interpreting TSA results from real CFRP components with complex layups and uncertain material data. It has shown that the model is useful even when an average ply thickness is employed and the material properties used as model inputs are for a typical carbon fibre composite, rather than the exact material choice. The ability to extract a simple test specimen has been vital in proving the model provides realistic results and could be applied to a wide range of stacking sequences to identify at which loading frequency the specimen should be tested. Moreover, if the loading frequency is restricted to a certain range the model enables a better understanding of the thermodynamic conditions generated by the loading. The ability to estimate the onset of adiabatic conditions corroborates the applicability of the modelling framework to aerospace structural composites. This is a significant outcome, since it supports its use in TSA-based structural assessments, predictive validation, and virtual testing workflows, even when detailed material characterisation is impractical or unavailable.

10. Conclusions

A comprehensive experimental validation of a FEM modelling framework that simulates the effect of ply by ply heat transfer on the thermoelastic response has been presented. The modelling framework is particularly applicable to CFRP laminated composite materials. The validation study demonstrated that the model accurately captures the complex heat transfer in multidirectional laminates. The validation comprised 72 experimental cases achieved through a variety of laminate stacking sequences and by changing the cyclic loading frequencies to generate different heat transfer scenarios. It was demonstrated that the FEM model framework could incorporate the resin rich surface layer generated during manufacturing. The model was also able to simulate the thermal damping effect of the paint coating used to provide a uniform emissivity in infrared thermography.

Once validated, it was demonstrated that the modelling framework was able to predict the thermoelastic response from the subsurface plies, providing a means of interpreting the experimental results from the surface over a range of loading frequencies. The model revealed how the thermoelastic heat source and heat transfer gradients evolve through the laminate thickness with differing loading frequencies. It was demonstrated that the phase plays an important role in determining the onset of adiabatic conditions. A particularly important result is that the model demonstrates that fully adiabatic behaviour generated only by the thermoelastic coupling is achieved when the phase value is either 0 or 180°.

The validation study revealed that for resin dominated stacking sequences, such as the $[\pm 45]_{3s}$, some model refinement is necessary, which includes incorporating the effect of intrinsic dissipation and the temperature dependence of the elastic constants. The latter will require a detailed experimental characterisation of the material behaviour. The applied strains used in the study of the $[\pm 45]_{3s}$ were relatively large, and it was shown that viscoelastic effects occurred at around a loading frequency of 16 Hz; it is unlikely that such high loading frequencies and strains would be used during testing of actual composite components. In most cases the spatial averaging of the experimental data was sufficient to account for the inhomogeneity of the distribution of the fibres in the resin. However an avenue for further refinement of the FEM modelling framework would be to account for this in the model, the key challenge being maintaining computational efficiency.

The validated FEM modelling framework enabled a parametric study of the effect of the paint coating. This confirmed that the paint attenuates the thermoelastic response by introducing a phase delay caused by thermal damping. In contrast, a parametric study of resin rich surface layer thickness, showed that it fundamentally modifies the through-thickness heat transfer characteristics. Furthermore, it was demonstrated that even very thick surface resin rich layers do not act as a strain witness in CFRP materials. To eliminate effects of heat transfer to the surface, an unrealistically thick resin rich surface layer (> 125 μm) would be required. Instead, the results of the parametric study suggest that using a homogenised global response from specimens loaded at low frequencies may be a more practical alternative for TSA on actual structural components. However, this is yet to be demonstrated on specimens where the in-plane stress field is varying, such as at holes for fastener locations and situations where damage is evolving.

Two case studies were presented, the first demonstrated the applicability of the FEM model framework on an industrially relevant quasi-isotropic laminate ($[0/90/45/-45]_s$). A key outcome was that for low loading frequencies the thermoelastic response is largely insensitive to RRL variation. It was shown that adiabatic conditions cannot be achieved at loading frequencies of less than 20 Hz for laminates with plies having ~ 125 μm thickness. The results demonstrate strongly that the FEM model framework is required to understand the thermodynamic condition of a structure and conduct an experiment where reliable and quantitative data could be obtained under low-frequency loading conditions in realistic composite structures. The second case study established the utility of the FEM model in understanding the response from a component with unknown material properties. The model replicated the response of a coupon extracted from a real CFRP component, with uncharacterised material properties.

Future work that utilises the FEM modelling framework is as follows:

- Investigating configurations such as open hole structures where additional in-plane heat transfer occurs, as well as non-uniform stress fields in each ply,
- Supporting the identification of the evolution of subsurface damage using TSA, by using the FEM model to identify a loading frequency where the surface response is dominated by a subsurface ply.
- Calibrating the use of the homogenised response at low frequencies and applying to large CFRP structural tests.

CRediT authorship contribution statement

Riccardo Cappello: Writing – review & editing, Writing – original draft, Visualization, Validation, Methodology, Investigation, Formal analysis, Data curation, Conceptualization. **Rafael Ruiz-Iglesias:** Writing – original draft, Visualization, Validation, Methodology, Investigation, Formal analysis, Data curation, Conceptualization. **Giuseppe Pitarresi:** Writing – review & editing, Supervision, Methodology, Investigation, Conceptualization. **Giuseppe Catalanotti:** Writing – review & editing, Supervision, Methodology, Investigation, Funding acquisition, Conceptualization. **Janice M. Dulieu-Barton:** Writing – review & editing, Supervision, Methodology, Investigation, Funding acquisition, Conceptualization, Writing – original draft.

Declaration of competing interest

The authors declare that they have no known competing financial interests or personal relationships that could have appeared to influence the work reported in this paper.

Acknowledgments

The work presented in this paper was supported by the EPSRC Programme Grant 'Certification for Design – Reshaping the Testing Pyramid' (CerTest, EP/ S017038/1).

Appendix 1

.

Table A1
Average longitudinal strain from each test and layup from dic.

Loading frequency [Hz]	Avg. strains for each test and layup [με]				
	$[0/90]_{3s}$	$[90/0]_{3s}$	$[\pm 45]_{3s}$	$[0/45/-45/0/0/0]_s$	$[0/0/0/45/-45/0]_s$
0.5	–	–	–	2050	1926
1.1	1770	1509	4257	2049	1924
2.1	–	–	–	2049	1926
3.1	1600	1511	4189	2051	1921
4.1	–	–	–	2050	1922
5.1	1497	1499	4154	2047	1911
6.1	–	–	–	2044	1905
7.1	1489	1523	4132	2040	1899
8.1	–	–	–	2036	1891
9.1	–	–	–	2031	1876
10.1	1494	1546	4112	2029	1870
12.1	1513	1600	4075	2011	1844
15.1	1614	1630	4037	1987	1797
17.1	–	–	–	1968	1770
20.1	1634	1692	4013	1937	1701
22.1	1592	1731	3996	1925	1721
25.1	1643	1690	3928	1790	1673
27.1	1684	1657	3941	1905	1610
30.1	1633	1686	3950	2021	1551

Data availability

Data will be made available on request.

References

[1] Thomson II W. On the thermoelastic, thermomagnetic, and pyroelectric properties of matter. The London, Edinburgh, and Dublin Philosophical Magazine and Journal of Science Taylor & Francis 1878;5(28):4–27.
[2] Dulieu-Barton JM. Thermoelastic stress Analysis. Optical Methods for Solid Mechanics. Wiley-VCH 2012:345–66.
[3] Stanley P., Chan WK. The application of thermoelastic stress analysis techniques to composite materials. The Journal of Strain Analysis for Engineering Design. SAGE Publications Sage UK: London, England; 1988; 23(3): 137–143.
[4] Jiménez-Fortunato I, Devivier C, Dulieu-Barton JM. Assessment of microbolometer infrared cameras for thermoelastic stress analysis. Strain Wiley Online Library 2025;61(1):e12493.
[5] Wong AK. A non-adiabatic thermoelastic theory for composite laminates. Phys Chem Solids Elsevier 1991;52(3):483–94.
[6] Pitarresi G, Galietti U. A quantitative analysis of the thermoelastic effect in CFRP composite materials. Strain Wiley Online Library 2010;46(5):446–59.
[7] Jiménez-Fortunato I, Bull DJ, Thomsen OT, Dulieu-Barton JM. On the source of the thermoelastic response from orthotropic fibre reinforced composite laminates. Compos Part A Appl Sci Manuf Elsevier 2021;149:106515.
[8] de Sá Rodrigues F, Marques R, Tabrizi IE, Kefal A, Ali HQ, Yildiz M, et al. A new methodology for thermoelastic model identification in composite materials using digital image correlation. Opt Lasers Eng Elsevier 2021;146:106689.
[9] Cappello R, Pitarresi G, Catalanotti G. Thermoelastic stress Analysis for composite laminates: a numerical investigation. Composites Science and Technology Elsevier 2023;241:110103.
[10] Hexcel. HexPly® 8552 Product data. https://www.hexcel.com/Resources/DataSheets/Prepreg. 2023.
[11] Pitarresi G, Conti A, Galietti U. Investigation on the influence of the surface resin rich layer on the thermoelastic signal from different composite laminate lay-ups. Appl Mech Mater 2005:167–72.
[12] Emery TR, Dulieu-Barton JM, Earl JS, Cunningham PR. A generalised approach to the calibration of orthotropic materials for thermoelastic stress analysis. Compos Sci Technol Elsevier 2008;68(3–4):743–52.
[13] Ruiz-Iglesias R., Cappello R., Thomsen OT., Dulieu-Barton JM. Estimating the coefficients of thermal expansion of carbon fibre composite materials using infrared thermography. Composites Part A: Applied Science and Manufacturing. Elsevier Ltd; 1 November 2025; 198. Available at: DOI:10.1016/j.compositesa.2025.109094.
[14] Lemaitre J. Chaboche J-L. Mechanics of Solid Materials: Cambridge University Press; 1994.
[15] Chrysochoos A, Louche H. An infrared image processing to analyse the calorific effects accompanying strain localisation. Int J Eng Sci Elsevier 2000;38(16):1759–88.
[16] Wong AK, Sparrow JG, Dunn SA. On the revised theory of the thermoelastic effect. Phys Chem Solids Elsevier 1988;49(4):395–400.
[17] Potter RT, Greaves LJ. The application of thermoelastic stress analysis techniques to fibre composites. Optomechanical. Syst Eng 1987:134–46.
[18] Dunn SA. Analysis of thermal conduction effects on thermoelastic temperature measurements for composite materials. Journal of Applied Mechanics. (59(3)):552–558. Available at: doi 1992;10(1115/1):2893759.

[19] Crump DA., Dulieu-Barton JM. Assessment of Non-adiabatic Behaviour in Thermoelastic Stress Analysis of Composite Sandwich Panels. Experimental Mechanics. Springer Science and Business Media, LLC; 1 September 2012; 52(7): 829–842. Available at: DOI:10.1007/s11340-012-9601-9.
[20] Bakis CE., Reifsnider KL. The adiabatic thermoelastic effect in laminated fiber composites. J Compos Mater. Sage Publications Sage UK: London, England; 1991; 25(7): 809–830.
[21] Van Hemelrijck D, Schillemans L, Cardon AH, Wong AK. The effects of motion on thermoelastic stress analysis. Compos Struct Elsevier 1991;18(3):221–38.
[22] Pitarresi G, Found MS, Patterson EA. An investigation of the influence of macroscopic heterogeneity on the thermoelastic response of fibre reinforced plastics. Compos Sci Technol Elsevier 2005;65(2):269–80.
[23] Zhang D., Enke NF., Sandor BI. Thermographic stress analysis of composite materials. Experimental Mechanics. March 1990; 30(1): 68–73. Available at: DOI: 10.1007/BF02322705.
[24] Rajic N, Rowlands D. Thermoelastic stress analysis with a compact low-cost microbolometer system. Quantitative infrared thermography journal. Taylor & Francis 2013;10(2):135–58.
[25] Pitarresi G, Cappello R, Catalanotti G. Quantitative thermoelastic stress analysis by means of low-cost setups. Opt Lasers Eng Elsevier 2020;134:106158.
[26] Thatcher JE., Crump DA., Devivier C., Bailey PBS., Dulieu-Barton JM. Low cost infrared thermography for automated crack monitoring in fatigue testing. Optics and Lasers in Engineering. March 2020; 126: 105914. Available at: DOI:10.1016/j.optlaseng.2019.105914.
[27] Laux T, Cappello R, Callaghan JS, Ólafsson G, Boyd SW, Crump DA, et al. Integrated testing and modelling of substructures using full-field imaging and data fusion. Engineering Structures Elsevier 2025;324:119338.
[28] Camanho PP, Maimi P, Dávila CG. Prediction of size effects in notched laminates using continuum damage mechanics. Compos Sci Technol Elsevier 2007;67(13): 2715–27.
[29] Catinaccio A, Magnet EJH, Cfrp,. Available at: Casing Conceptual Study 2021. https://indico.cern.ch/event/993477/contributions/4177767/attachments/2175199/3673447/HTS_magnet_conceptual_study_JE_draftV6_21-1-2021.pdf.
[30] Zhang B., Kawashita LF., Jones MI., Lander JK., Hallett SR. An experimental and numerical investigation into damage mechanisms in tapered laminates under tensile loading. Composites Part A: Applied Science and Manufacturing. June 2020; 133: 105862. Available at: DOI:10.1016/j.compositesa.2020.105862.
[31] Kaddour A., Hinton M., Smith P., Li S. Mechanical properties and details of composite laminates for the test cases used in the third world-wide failure exercise. Journal of Composite Materials. 19 September 2013; 47(20–21): 2427–2442. Available at: DOI:10.1177/0021998313499477.
[32] Daynes S, Potter KD, Weaver PM. Bistable prestressed buckled laminates. Compos Sci Technol December 2008;68(15–16):3431–7. https://doi.org/10.1016/j.compscitech.2008.09.036. Available at:.
[33] Stacey JP, O'Donnell MP, Schenk M. Thermal Prestress in Composite Compliant Shell Mechanisms. In: Volume 5A: 42nd Mechanisms and Robotics Conference. American Society of Mechanical Engineers; 2018. https://doi.org/10.1115/DETC2018-85826.
[34] Johnston AA. An integrated model of the development of process-induced deformation in autoclave processing of composite structures. University of British Columbia; 1997.
[35] Sutton MA., Orteu J-J., Schreier HW. Image Correlation for Shape, Motion and Deformation Measurements Basic Concepts, Theory and Applications, Springer.
[36] Battams GP, Dulieu-Barton JM. Data-rich characterisation of damage propagation in composite materials. Composites Part a: Applied Science and Manufacturing. Elsevier Ltd December 2016;1(91):420–35. https://doi.org/10.1016/j.compositesa.2016.08.007. Available at:.
[37] MatchID [Online]. https://www.matchid.eu/.
[38] Fruehmann RK, Dulieu-Barton JM, Quinn S, Tyler JP. The use of a lock-in amplifier to apply digital image correlation to cyclically loaded components. Optics and Lasers in Engineering Elsevier 2015;68:149–59.
[39] Robinson AF., Dulieu-Barton JM., Quinn S., Burguete RL. Paint coating characterization for thermoelastic stress analysis of metallic materials. Measurement Science and Technology. 1 August 2010; 21(8): 085502. Available at: DOI:10.1088/0957-0233/21/8/085502.
[40] Raghu O., Philip J. Thermal properties of paint coatings on different backings using a scanning photo acoustic technique. Measurement Science and Technology. 1 November 2006; 17(11): 2945–2949. Available at: DOI:10.1088/0957-0233/17/11/012.
[41] Dunn SA., Lombardo D., Sparrow JG. The Mean Stress Effect in Metallic Alloys and Composites. In: Stanley P (ed.) 1989. p. 129. Available at: DOI:10.1117/12.952913.
[42] Certification for design: Reshaping the testing pyramid. https://www.composites-certest.com/.